eChem
https://www.sciltp.com/journals/eChem

Review

Rational Design of Nano and Atomically Dispersed Catalysts for Electrocatalytic Ammonia Synthesis from Nitrate

Ziteng Zhang †, Zhiyi Sun †, Zihao Wei *, Zhuo Chen *, Qi Sun, Ziheng Zhan, Xuecong Li, Aoxue Huang, Shenghua Li *, Wenxing Chen * and Siping Pang *

School of Materials Science and Engineering, Beijing Institute of Technology, Beijing 100081, China
* Correspondence: weihongyuan99@126.com (Z.W.); zchen@bit.edu.cn (Z.C.); lishenghua@bit.edu.cn (S.L.); wxchen@bit.edu.cn (W.C.); pangsp@bit.edu.cn (S.P.)
† These authors contributed equally to this work.

How To Cite: Zhang, Z.; Sun, Z.; Wei, Z.; et al. Rational Design of Nano and Atomically Dispersed Catalysts for Electrocatalytic Ammonia Synthesis from Nitrate. *eChem* **2025**, *1* (1), 2. https://doi.org/10.53941/echem.2025.100002.

Received: 17 August 2025
Revised: 12 September 2025
Accepted: 25 September 2025
Published: 28 September 2025

Abstract: Ammonia is a vital industrial feedstock and a carbon-free hydrogen carrier, yet the conventional Haber–Bosch process requires extreme temperatures and pressures and produces substantial CO_2 emissions, rendering its large-scale operation energy-intensive and environmentally unsustainable. Electrochemical nitrate reduction (NO_3RR) has emerged as a promising alternative, benefiting from the relatively low N=O bond dissociation energy and the high solubility of nitrate ions in aqueous media. This approach not only enables ammonia production under ambient conditions but also provides a sustainable pathway for nitrate wastewater remediation, thereby addressing two pressing global challenges simultaneously. In this review, we present a comprehensive overview of recent advances in NO_3RR catalyst development, with particular emphasis on two major classes: nanocrystalline catalysts and atomically dispersed catalysts. Nanocrystalline systems leverage tunable parameters such as crystal facet exposure, lattice strain, defect density, and heteroatom doping to regulate adsorption energies, enhance intermediate activation, and reconcile competing reaction pathways. Atomically dispersed catalysts—including single-atom, dual-atom, and sub-nanometer cluster architectures—achieve nearly complete atomic utilization while offering precisely defined active sites that serve as model platforms for probing structure–activity relationships. Together, these two categories represent complementary strategies: nanocrystals emphasize mesoscale control of morphology and electronic structure, whereas atomic-level catalysts advance the frontier of precision design and mechanistic understanding. We highlight the critical role of *in situ* and *operando* characterization in capturing dynamic transformations. Finally, this review discusses the challenges and opportunities that remain for translating these fundamental advances into scalable, efficient, and sustainable electrocatalytic ammonia synthesis.

Keywords: nanocrystalline catalysts; atomically dispersed catalysts; electrocatalytic nitrate reduction; *in situ* characterization

1. Introduction

Ammonia is among the most extensively produced industrial chemicals worldwide, with approximately 80% of the total output utilized in agriculture for fertilizer manufacturing [1,2]. Beyond its traditional agricultural applications, ammonia's high energy density, carbon-free composition, and rich hydrogen content have positioned it as a promising hydrogen carrier and energy storage medium, drawing increasing attention in the energy sector

[3,4]. Industrial synthesis predominantly relies on the conventional Haber–Bosch process, in which nitrogen and hydrogen are converted into ammonia. The dissociation of the N≡N triple bond in molecular nitrogen requires substantial energy (941 kJ mol^{-1}), necessitating reaction conditions of elevated temperature (350–500 °C) and high pressure (15–30 MPa). As a result, global ammonia production accounts for 1–2% of annual energy consumption and emits over 400 million tons of CO_2 each year, a profile that fundamentally conflicts with dual-carbon strategic objectives [5]. Despite its industrial maturity, the Haber–Bosch process faces critical challenges when viewed from the perspective of sustainable development. The high energy input and carbon footprint hinder alignment with net-zero emission goals, while its reliance on centralized, large-scale facilities limits flexibility for distributed or small-scale ammonia production [6]. Furthermore, in practical industrial operation, issues such as catalyst deactivation, the need for frequent regeneration, and the high costs associated with CO_2 capture and storage further complicate the transition toward greener ammonia synthesis [7]. These challenges underscore the urgent need for alternative strategies, such as electrochemical nitrate reduction, that can operate under mild conditions with lower energy requirements while simultaneously addressing environmental concerns.

Given the limitations of the traditional Haber–Bosch process, it is imperative to develop innovative ammonia production technologies that operate under mild conditions and are environmentally sustainable. As illustrated in Figure 1, extensive research has been devoted to ammonia (NH_3) synthesis [8–17]. Among the various strategies, electrochemical approaches have garnered considerable attention owing to their low cost, high efficiency, mild operating requirements, and green synthesis potential. These methods are primarily classified into electrocatalytic nitrogen reduction (NRR) and electrocatalytic nitrate reduction (NO_3RR) [8,9,18–26]. However, the extremely low solubility of N_2 in water and the high dissociation energy of the N≡N bond result in generally low Faradaic efficiency (FE) and ammonia yield for NRR. In contrast, nitrate possesses a lower N=O bond energy and high aqueous solubility, rendering electrocatalytic NO_3^--to-NH_3 conversion more feasible than NRR [27]. Moreover, nitrate pollutants are widely present in domestic and industrial wastewater, causing severe environmental degradation and posing significant risks to human health [28–30]. Electrocatalytic nitrate reduction, when powered by renewable electricity, offers the dual benefit of ammonia synthesis and wastewater remediation with comparatively high reaction efficiency, while enabling waste valorization [31]. Consequently, NO_3RR represents a promising alternative to the Haber–Bosch process, aligning with the principles of sustainable and green development.

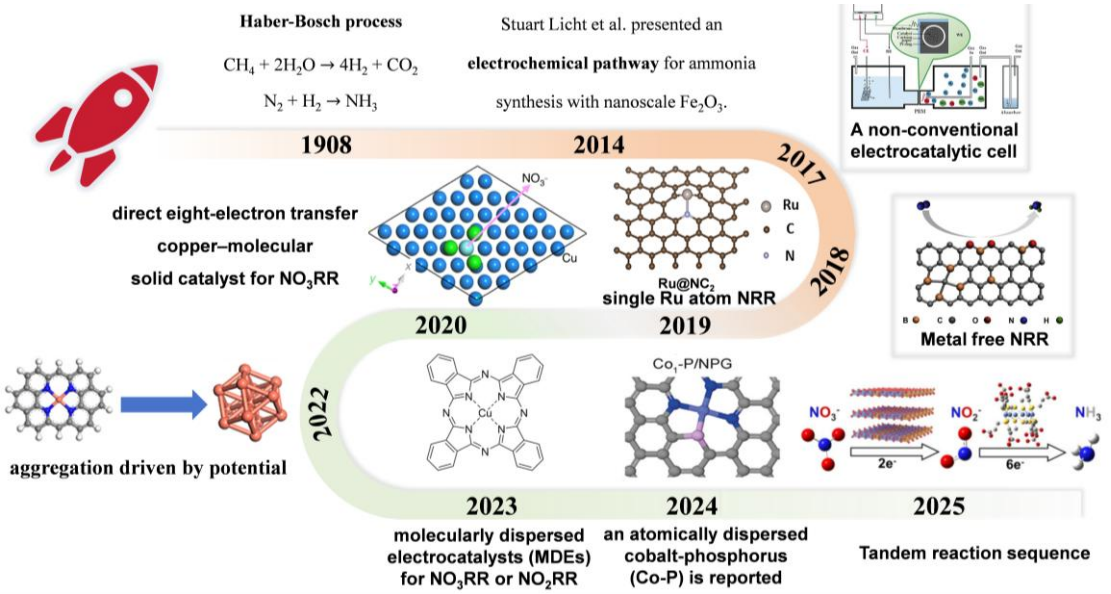

Figure 1. A brief history of the development and the latest progress of NH_3 synthesis from 1908 to 2025. Reproduced with permission. Copyright 2017 Wiley-VCH Verlag GmbH & Co. KGaA, Weinheim. Copyright 2018 with permission from Elsevier. Copyright 2019, with permission from Elsevier. Copyright 2020 Springer Nature. Copyright 2022 American Chemical Society. Copyright 2023 Royal Society of Chemistry. Copyright 2024 Wiley-VCH GmbH. Copyright 2025 American Chemical Society.

Despite its promise, the NO_3RR-to-NH_3 system still encounters several formidable challenges. First, the reaction proceeds via a complex multi-step electron–proton coupled transfer pathway, generating a variety of intermediates whose non-selective conversion often diminishes ammonia yield and selectivity [32−37]. Second,

the modulation principles governing both reaction kinetics and catalytic performance remain elusive; mass-transfer limitations further constrain reaction rates, and the long-term stability of catalysts is hindered by structural reconstruction or chemical corrosion of active sites [38–41]. Most critically, the interfacial interaction mechanisms between NO_3RR electrocatalysts and nitrate ions—encompassing adsorption geometries, charge-transfer pathways, and intermediate evolution routes—are not yet fully understood, warranting systematic elucidation [42–47]. Against this backdrop, both nanocrystalline and atomic-level catalysts have garnered significant attention due to their complementary advantages in NO_3RR-driven ammonia synthesis [47–52]. Nanocrystalline catalysts, with their tunable lattice strain, crystallographic facet exposure, and defect chemistry, enable ensemble-level regulation of adsorption energetics—modulating intermediate activation and product release through strain–facet coupling [53–57]. This mesoscale structural versatility offers broad control over catalytic kinetics and selectivity while maintaining high structural stability under operating conditions. In parallel, atomic-level catalysts achieve exceptional atomic utilization efficiency, with precisely defined coordination environments that permit fine-tuning of electronic and geometric structures at the single-site scale [58–61]. Such well-defined active sites not only maximize intrinsic catalytic activity but also provide ideal model platforms for dissecting structure–activity relationships at the molecular level. Recent studies have spanned the full spectrum—from nanocrystals to single atoms, dual atoms, and small clusters—revealing diverse yet interconnected strategies to regulate activity and selectivity, often integrating strain engineering, facet control, and local coordination design. This review focuses on NO_3RR electrocatalysts across these scales, categorized into nanocrystalline, single-atom, dual-atom, and cluster systems (Figure 2). We summarize their underlying mechanisms, regulation strategies, and *operando*/*in situ* characterization insights, complemented by theoretical calculations, and conclude with future research directions to guide the rational design of next-generation nitrate reduction electrocatalysts.

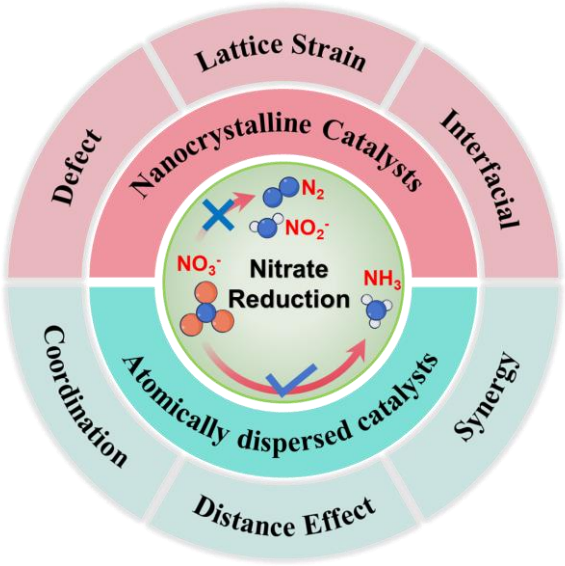

Figure 2. An overview of the main content for the review.

2. Mechanism of NO_3RR to Ammonia

Electrocatalytic NO_3RR is an intricate proton–electron coupled process that involves the transfer of eight electrons and nine protons, ultimately producing ammonia from nitrate. In acidic and neutral electrolytes, the overall reaction can be represented as:

$$NO_3^- + 9H^+ + 8e^- \rightarrow NH_3 + 3H_2O$$

In alkaline electrolytes:

$$NO_3^- + 6H_2O + 8e^- \rightarrow NH_3 + 9OH^-$$

Given the large number of intermediates generated during NO_3RR [62,63], elucidating the precise reaction sequence on the electrode surface remains a formidable challenge. The diversity and transient nature of these intermediates strongly influence the reaction pathway, thereby governing the final product distribution (Figure 3). Consequently, achieving high NH_3 selectivity is not only a key performance indicator but also a central design objective for NO_3RR electrocatalysts.

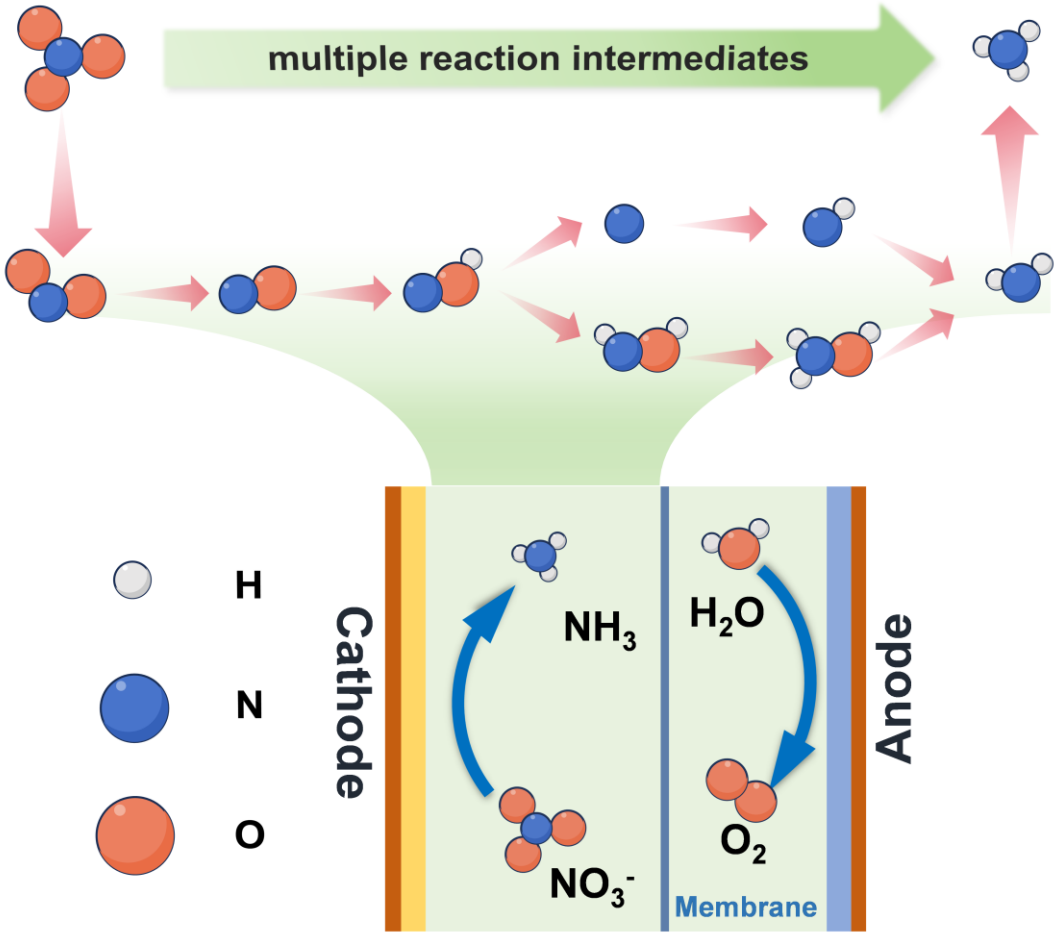

Figure 3. Two main pathways of NO_3RR to NH_3.

2.1. Indirect and Direct Mechanistic Regimes

NO_3RR to NH_3 can proceed via indirect or direct pathways, with the dominant route determined by nitrate concentration and electrolyte pH [64–66]. Indirect pathway: Predominant under high nitrate concentrations (>1 mol L^{-1}) and strongly acidic conditions, this route circumvents direct electron transfer to NO_3^-. Instead, reactive nitrogen species such as NO_2 or NO^+ serve as the primary electron acceptors in the catalytic cycle. In the Vetter mechanism, protonation of adsorbed NO_2^- produces HNO_2, which reacts with HNO_3 to yield H_2O and N_2O_4; the latter is subsequently reduced, regenerating NO_2. In the Schmid mechanism, NO^+—formed via HNO_2 protonation—acts as the key reactive intermediate, with continuous HNO_2 regeneration sustaining the cycle. Direct pathway: More relevant for electrocatalytic NH_3 synthesis under practical conditions (<1 mol L^{-1} nitrate), the direct route can be further classified into electron-mediated and H_{ads}-mediated reductions. In the electron-mediated pathway, NO_3^- and its successive intermediates undergo direct multi-electron transfer steps at the catalyst surface. In contrast, the H_{ads}-mediated pathway involves hydrogen atoms adsorbed on the catalyst surface acting as the primary reductants, sequentially hydrogenating intermediates toward NH_3 formation. The relative contribution of each sub-pathway is governed by catalyst surface structure, electronic properties, and the local reaction microenvironment.

In the electron-mediated pathway, NO_3^- first adsorbs onto the catalyst surface ($*NO_3$) and is reduced to $*NO_2$, a widely recognized rate-determining step (RDS) [67,68]. The $*NO_2$ intermediate undergoes further reduction to *NO, which is pivotal in dictating the ultimate product distribution [69–72]. Strong adsorption of *NO favors its stepwise hydrogenation to *HNO, $*H_2NO$, $*NH_2NO$, and eventually NH_3. However, *NO can also desorb into the electrolyte as NO(aq) or couple with adjacent *NO species to generate N_2O, which is subsequently reduced to N_2, thereby diverting the reaction toward undesired byproducts. For the H_{ads}-mediated process, surface-adsorbed hydrogen is generated via the Volmer step of water electrolysis. H_{ads} reduces nitrate along the sequence $*NO_2 \rightarrow *NO \rightarrow *N \rightarrow *NH \rightarrow *NH_2$, ultimately forming NH_3. While N_2 can form via N–N coupling of *N species, the faster kinetics of N–H bond formation generally favor ammonia production. This pathway is often observed at low overpotentials, which also suppresses competing reactions.

2.2. Competition with the Hydrogen Evolution Reaction (HER)

The primary competing reaction in NO_3RR is the HER, which proceeds via a simple two-electron transfer:

$$2H^+ + 2e^- \rightarrow H_2$$

HER typically exhibits lower kinetic barriers than NO_3RR, particularly in acidic electrolytes, and competes for both protons/electrons and adsorption sites on the catalyst surface [65,71]. In acidic media, the high proton concentration promotes rapid formation of *H, which may participate in hydrogenation steps of NO_3RR but more often recombines to form H_2, thereby suppressing NH_3 yield.

Considering the above mechanistic insights, two aspects are particularly important for steering NO_3RR selectivity toward NH_3. (1) The adsorption strength of key NO_x intermediates, especially *NO_2 and *NO, must be tuned to promote their sequential hydrogenation while preventing premature desorption or conversion to N_2O; (2) a balanced supply of reactive hydrogen species should be sustained to drive nitrate reduction, while avoiding excessive *H coverage that would divert electrons toward the competing HER pathway. These principles provide a unifying framework for the rational design of both atomically dispersed and nanocrystalline catalysts. The former enables precise control over local coordination environments at the atomic level, while the latter offers structural tunability through facet orientation, defect regulation, and interfacial modulation. Together, they open broad opportunities for tailoring catalytic surfaces to guide intermediate evolution and optimize selectivity in NO_3RR systems.

3. Nanocrystalline Catalysts for NO_3RR

Nanocrystalline catalysts have emerged as promising candidates for electrocatalytic NO_3RR owing to their highly tunable crystal facets, abundant density of surface-active sites, and superior charge transport properties [72–75]. Rational modulation of their structural attributes enables precise control over the adsorption configuration and binding strength of reaction intermediates, optimizes coupled electron–proton transfer kinetics, and mitigates competitive side reactions [76–78]. This section highlights recent advances in nanocrystalline NO_3RR catalysts, with emphasis on the structure–activity relationships governed by defect engineering, lattice strain modulation, particle size effects, crystal facet exposure, and interfacial or synergistic coupling effects.

3.1. Defect Engineering

Defect engineering fundamentally reshapes the electronic structure and coordination environment of nanocrystals by introducing mid-gap states and shifting the Fermi level, thereby modulating metal–ligand bonding. Point defects—such as oxygen vacancies, dislocations, and edge sites—can enhance the adsorption of nitrate-derived intermediates (*NO_3, *NO_2), lower activation barriers (e.g., *NO_3 → *NO_2), and tune *NO binding to favor hydrogenation over undesired N–N coupling [79–82]. Both experimental and computational studies indicate that an optimal defect density maximizes activity while preventing excessive stabilization of intermediates, which can promote byproduct formation (e.g., N_2O). This trend is exemplified in plasma-derived $MnCuO_x$ catalysts with tunable oxygen vacancy concentrations (FE up to ~86%) [83] and in Cu_2O-based systems [84]. Under cathodic polarization, defect populations can dynamically form or heal, actively redirecting reaction pathways. The integration of *operando* spectroscopies with DFT calculations provides a quantitative framework to correlate defect characteristics with catalytic selectivity and durability [85,86].

Point defects—particularly oxygen vacancies—reshape nanocrystal electronic structure by introducing localized states near the Fermi level and redistributing charge around under-coordinated metal sites. In NO_3RR, such modifications lower the activation barrier for the *NO_3 → *NO_2 step, tune *NO and *H adsorption energetics, and shift the balance between hydrogenation and N–N coupling pathways [87–89]. Converging experimental and theoretical studies reveal that ordered vacancy layers can even impart metallic surface character to semiconducting oxides, thereby accelerating interfacial electron transfer—a rate-limiting step in multi-electron nitrate reduction. Recent mechanistic frameworks conceptualize vacancies as a key lever to decouple the activation of early intermediates (*NO_3/*NO_2) from the selectivity-governing steps (*NO hydrogenation vs. desorption/coupling), offering a route to simultaneously boost activity and selectivity [90–92].

Canonical experimental evidence comes from vacancy-rich TiO_2 nanotube arrays, where oxygen vacancies (O_v) markedly boost FE and ammonium selectivity. *Operando* and *ex situ* spectroscopies—e.g., Ti^{3+} signatures in X-ray photoelectron spectroscopy (XPS)/electron paramagnetic resonance (EPR) and O-defect peaks in Raman—correlate these vacancies with strengthened nitrate/nitrite adsorption and suppressed competitive H adsorption on TiO_2, steering the pathway toward stepwise hydrogenation rather than N_2O/N_2 formation (Figure 4a) [93,94].

Vacancy stabilization strategies follow the same mechanistic logic: dilute Cu incorporation promotes O_v generation and enhances electronic conductivity, weakening the N–O bond in the $*NO_3 \rightarrow *NO_2$ transition state while avoiding *NO over-stabilization that could divert the reaction toward coupling pathways. Perovskite oxides provide a complementary platform where A-site deficiency, hetero-cation substitution, and polarity inversion tune O_v formation energies and densities. In vacancy-enriched $LaFeO_{3-\delta}$, elevated NH_3 yields and Faradaic efficiencies are consistently linked—via EPR, XPS, and O K-edge analyses—to abundant O_v sites that anchor NO_x intermediates and facilitate proton-coupled electron transfer (Figure 4b) [95–97]. Mechanistically, these oxides integrate Lewis-acidic B-sites for NO_x binding/activation with adjacent O_v sites that lower the barrier for N–O bond cleavage and subsequent hydrogenation, creating a dual-site catalytic effect intrinsic to the perovskite lattice under cathodic bias.

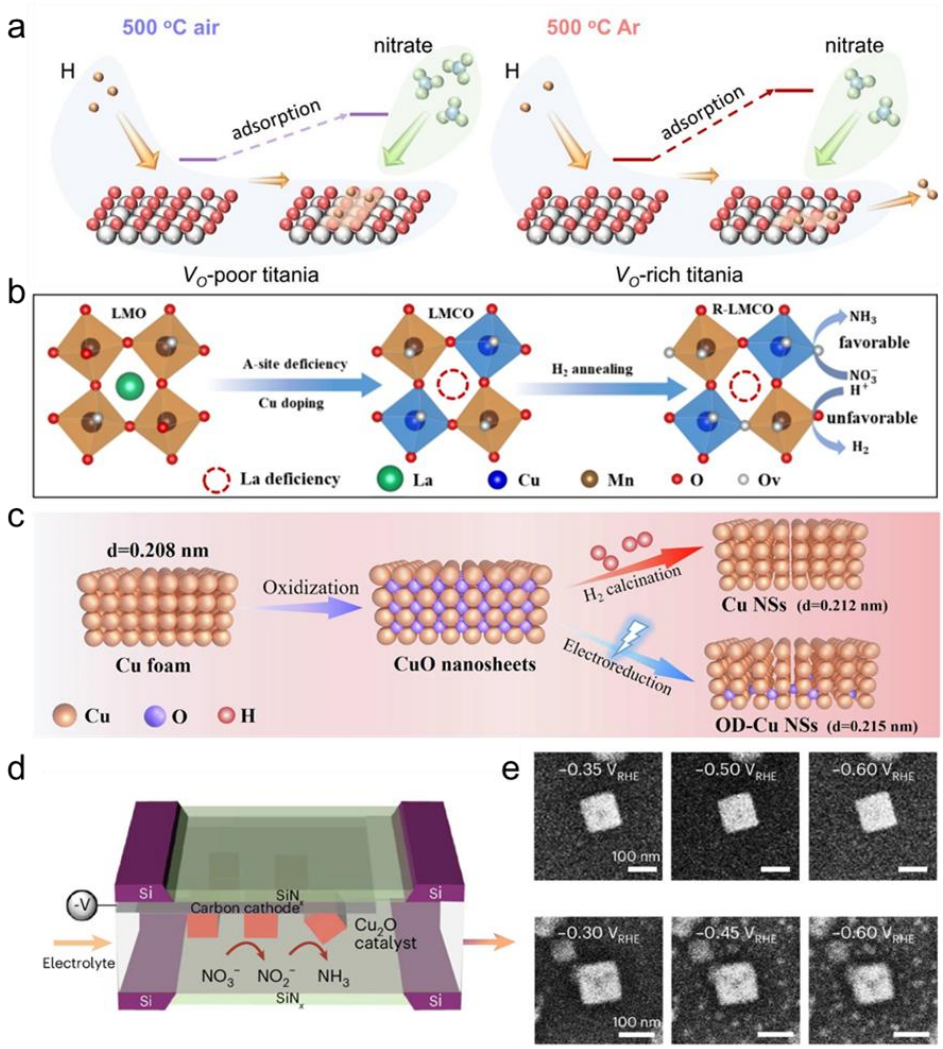

Figure 4. (**a**) Illustration of the hydrogen adsorption behavior at a lower voltage. With fewer V_O, a hydrogen or hydrogen bond network is formed on the surface of titania, which further provides a hydrogen-rich environment for nitrate reduction. Gray and red spheres represent Ti and O atoms of titania, while brown, blue, and green spheres stand for H, N, and O of nitrate. The step diagram is a schematic diagram of the energy change before and after hydrogen adsorption based on the above experimental results. Titania of 500 °C air-treated displays a lower energy barrier to adsorb hydrogen, while the 500 °C Ar-treated titania appears to favor the HER. Reproduced with permission [93]. Copyright 2024 with permission from the American Chemical Society. (**b**) Schematic synthetic procedure of LMO, LMCO, and R-LMCO. Reproduced with permission [95]. Copyright 2025 with permission from the American Chemical Society. (**c**) Schematic illustration of Cu NSs and OD-Cu NSs synthesis. Reproduced with permission [98]. Copyright 2025 with permission from Springer Nature. (**d**) Schematic of the EC-TEM experimental configuration in which the Cu_2O precatalyst was electrodeposited on the working electrode of an EC-TEM chip prior to the experiment. **(e)** Snapshots showing the restructuring of Cu_2O cubes as observed by operando EC-TEM during linear sweep voltammetry under NO_3RR conditions. Reproduced with permission [99]. Copyright 2025 with permission from Springer Nature.

In oxide-derived Cu-based catalysts, "vacancy-like" oxygen motifs inherited from oxide precursors act as sub-surface defect analogues that simultaneously mitigate intermediate poisoning and regulate hydrogen availability (Figure 4c) [98]. In Cu nanosheet arrays derived from oxide precursors, residual lattice oxygen weakens $*NO_2$ adsorption—avoiding site blockage—while tensile lattice strain accelerates water dissociation to supply *H (Figure 4d) [99]. This synergistic interplay delivers Faradaic efficiencies approaching 90–100% and high NH_3 productivity across a broad range of nitrate concentrations and current densities. Mechanistically, defect-type oxygen adjacent to Cu electronically attenuates $*NO_2$ binding, and the strained lattice sustains the hydrogenation sequence ($*NO \rightarrow *HNO \rightarrow *H_2NO \rightarrow NH_3$) without promoting excessive *H coverage that would favor the competing HER. Defects can also form and evolve dynamically under electrochemical bias [100]. In wide-bandgap oxides such as ZnO, intentional electroreduction ($ZnO \rightarrow ZnO_{1-x}$) generates oxygen vacancies *in situ*, enhancing conductivity, introducing new NO_x adsorption sites, and stabilizing hydrogenated intermediates—benefits retained if defect healing is kinetically hindered. On Cu, potential-induced restructuring produces vacancy- and adatom-rich oxide-derived surfaces that maintain high FE by pairing facile $*NO_2$ conversion with moderated *NO binding. These cases illustrate that "*operando* defects" are not incidental artifacts but tunable, performance-defining features that can be deliberately generated and preserved.

Taken together, these studies point to clear design heuristics for high-performance NO_3RR under practical conditions: (i) tune vacancy density to maximize $*NO_3/*NO_2$ activation without over-stabilizing *NO intermediates; (ii) integrate vacancy hosts with co-components—dopants or metallic domains—that supply *H while suppressing the HER; and (iii) secure long-term activity by tracking defect populations *operando* via X-ray absorption spectroscopy (XAS)/XPS, EPR, and vibrational spectroscopy, correlating these data with FE and partial current density under application-relevant loads [101–103]. Contemporary reviews distill these guidelines and recommend standardized protocols to quantitatively link defect characteristics with NO_3RR performance, providing a blueprint for rational catalyst design.

3.2. Lattice Strain Effects

Lattice strain and crystallographic facet exposure act as coupled structural levers that reshape the catalytic landscape in NO_3RR [104,105]. Strain engineering modifies metal–metal or metal–oxygen bond distances and alters local coordination symmetry, shifting the d-band center in metals or tuning metal–oxygen covalency in oxides [106]. These perturbations adjust the adsorption free energies of intermediates such as $*NO_2$ and *NO. Compressive strain generally upshifts the d-band, strengthening early-stage intermediate binding and facilitating $*NO_3/*NO_2$ activation, whereas tensile strain downshifts it, weakening binding and accelerating *NO desorption [107,108]. When optimized, strain can break the scaling relationship between $*NO_2$ and *NO adsorption, enabling simultaneous acceleration of activation kinetics and product-selective hydrogenation—a synergy confirmed by DFT and *operando* XRD/EXAFS studies that correlate lattice parameter shifts with coverage changes.

Facet exposure plays a pivotal role in modulating catalytic activity by dictating atomic arrangements, coordination geometries, and electronic structures. On metallic copper, low-index facets such as Cu(100) stabilize bridge-bound $*NO_2$ intermediates, facilitating hydrogenation toward NH_3, whereas the close-packed Cu(111) surface favors *NO desorption, thereby promoting N_2 and N_2O formation [109] (Figure 5a). For oxide catalysts, high-energy facets such as {001} or {110} present a greater density of coordinatively unsaturated sites and oxygen vacancies, which strengthen NO_3^- adsorption and lower activation barriers. *Operando* investigations further highlight the importance of facet stability: $Cu_2O(100)$ retains its binding energetics during prolonged operation, whereas the (111) facet undergoes surface reconstruction, diverting selectivity toward undesired products.

Representative cases illustrate how these structural effects operate in concert. In Ce-doped Co_3O_4 catalysts, gradient f–d–p orbital coupling introduced through Ce incorporation generates lattice strain that modulates the adsorption strengths of key NO_3RR intermediates (*H and *NO) in opposite directions [110]. This dual modulation breaks the conventional scaling relation that limits nitrate-to-ammonia electrosynthesis (Figure 5b–f). *Operando* and theoretical analyses show that the combined strain–orbital coupling lowers the energy barrier for *NO hydrogenation while suppressing the HER, achieving a FE of 97.8% and an NH_3 yield of 3423.0 $\mu g\ h^{-1}\ cm^{-2}$ under alkaline conditions. The catalyst also retains high activity across a wide NO_3^- concentration range (5–200 mM) and demonstrates excellent cycling stability, establishing gradient orbital coupling as a generalizable strategy—extendable to other lanthanide dopants such as Pr and Nd—for decoupling intermediate adsorption energetics and enhancing NO_3RR performance. A complementary approach is exemplified by FeTeSe nanosheets, where reaction-driven anisotropic lattice strains form *in situ* during NO_3RR [111]. Selective chalcogen leaching generates in-plane tensile and out-of-plane compressive components, distorting the lattice and enriching surface hydroxyl species (Figure 5g). These dynamic strains facilitate OH^-/NO_3^- co-adsorption and activation at strained Fe sites.

Operando synchrotron and theoretical investigations confirm that anisotropic strain reshapes the adsorption geometry and charge distribution of intermediates, yielding near-unity FE and an NH_3 production rate of ~42.1 mg h^{-1} mg_{cat}^{-1} even at low nitrate concentrations. This dynamic strain engineering thus complements static dopant-induced strain as a powerful route for boosting NO_3RR activity.

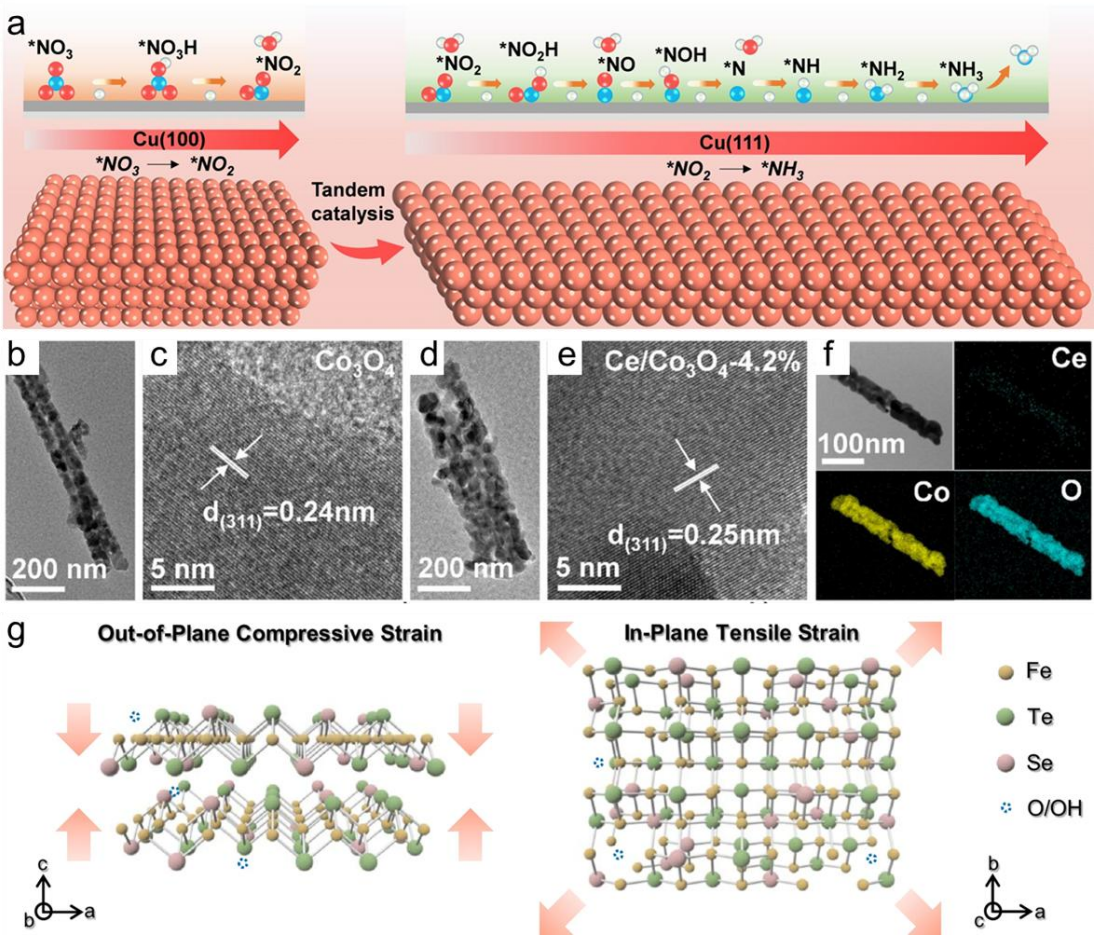

Figure 5. (**a**) Tandem interaction of Cu(100) and Cu(111) facets. Reproduced with permission [109]. Copyright 2023 with permission from Wiley-VCH GmbH. (**b**) TEM image and (**c**) HR-TEM image of Co_3O_4. (**d**) TEM image, (**e**) HR-TEM image, and (**f**) EDS image of Ce/Co_3O_4-4.2%. Reproduced with permission [110]. Copyright 2025 with permission from Wiley-VCH GmbH. (**g**) Schematic illustration of the FeTeSe crystal structure along the b and c directions, where the strain directions are indicated by the orange arrows. Reproduced with permission [111]. Copyright 2025 with permission from Springer Nature.

Overall, lattice strain–facet coupling offers a multidimensional design paradigm in which strain modulates the electronic structure, while facet exposure governs the spatial distribution of active sites. Future research should integrate quantitative strain mapping—such as Williamson–Hall analysis, GPA-HRTEM, and *operando* Raman spectroscopy—with facet-specific intermediate coverage profiling via SEIRAS, SHINERS, and time-resolved XAS to establish predictive structure–activity relationships. Such a combined approach will be essential for translating laboratory-scale performance gains into durable, high–current-density NO_3RR devices.

3.3. Interfacial and Synergistic Effects

Heterointerfaces induce charge redistribution, band bending, and dual-site reactivity, enabling the decoupling of activation from hydrogenation. Metallic domains can accelerate the $*NO_2 \rightarrow *NO$ conversion step, whereas oxophilic regions preferentially stabilize protonated intermediates. Interfacial spillover of *H or $*NO_x$ species shortens diffusion pathways and enhances reaction kinetics, while junctions can direct electron flow away from sites prone to the HER [112,113]. Elucidating the role of interfaces requires probing work-function variations, core-level shifts, and charge-transfer dynamics, whereas ensuring long-term performance demands preserving interfacial integrity under cathodic bias.

Heterointerfaces between distinct phases—such as metal/metal, metal/oxide, or oxide/oxide combinations—induce charge redistribution, band bending, and dual-site reactivity, all of which can strongly influence NO_3RR activity and selectivity. Electron-rich domains (e.g., metallic Cu or Pd) typically facilitate the $*NO_3 \rightarrow *NO_2$ conversion step, whereas adjacent oxophilic regions (e.g., metal oxides) preferentially stabilize and hydrogenate nitrogen–oxygen intermediates such as *NO and *HNO [114]. This spatial division of function decouples nitrate activation from hydrogenation, thereby suppressing the formation of N_2O and N_2. The Cu/Cu_2O interface exemplifies this concept (Figure 6a–d): metallic Cu sites accelerate electron transfer to $*NO_2$, while Cu_2O domains provide stronger adsorption for hydrogenated intermediates, collectively achieving Faradaic efficiencies exceeding 90% and high NH_3 partial current densities [115,116]. Interfacial engineering strategies also extend to multi-metal systems. Ordered B_2 CuPd intermetallic nanocubes display non-scaling adsorption behavior, where optimized bridge–bidentate $*NO_3$ binding on Cu sites couples with *N stabilization on Pd, yielding Faradaic efficiencies above 92% alongside long-term operational stability [117]. *Operando* X-ray absorption spectroscopy and Kelvin probe force microscopy confirm these interfacial electronic effects, revealing potential-dependent charge transfer and local work-function modulation.

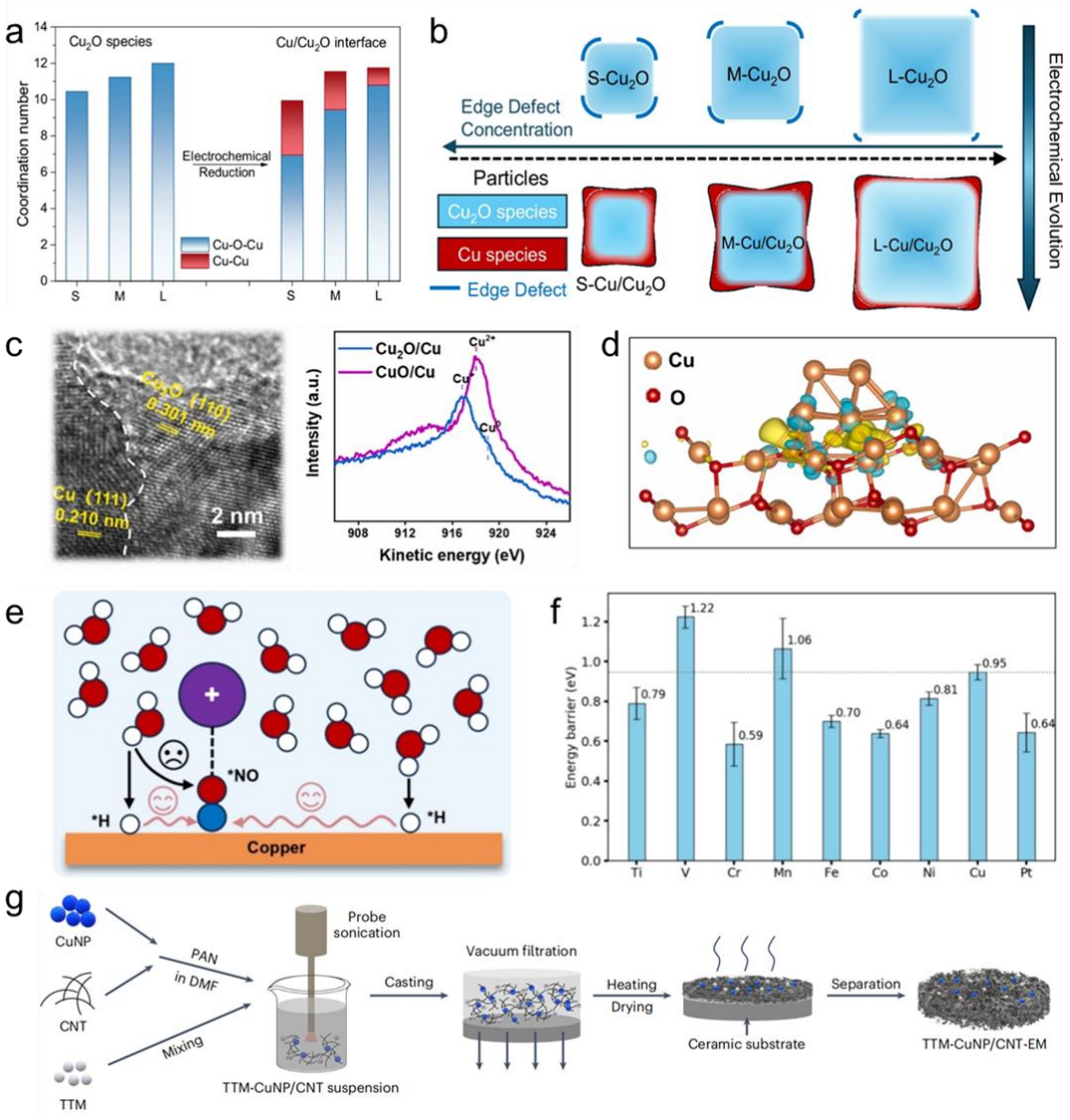

Figure 6. (**a**) Structural coherence changes in EXAFS coordination number of Cu–Cu bonds and Cu–O–Cu bonds. (**b**) Schematic diagram of structural transformation of Cu_2O with different sizes. (**c**) HRTEM and LMM AES spectra of CuO/Cu and Cu_2O/Cu interfaces. (**d**) Cu_2O/Cu electron cloud density. Reproduced with permission [114]. Copyright 2022 with permission from Springer Nature. (**e**) Schematic representation of the atomic mechanism elucidating the role of *H in regulating the NO_3RR reaction kinetics. (**f**) Energy barrier for the Volmer step on the MCu single atom alloys. Reproduced with permission [118]. Copyright 2024 with permission from the American Chemical Society. (**g**) schematic illustration of the TTM-CuNP/CNT-EM fabrication process. Reproduced with permission [42]. Copyright 2025 with permission from Springer Nature.

In aqueous NO_3RR, the HER inevitably competes for active sites, with *H generation in the Volmer step followed by Heyrovsky or Tafel steps leading to H_2 formation [118]. While high *H coverage generally accelerates HER, *H can also promote NO_3RR by hydrogenating oxygenated intermediates (*NO, *NO_2, *NO_3) through the Langmuir–Hinshelwood pathway. At the ion–water–interface nexus, alkali metal cations (e.g., K^+) strongly coordinate with these intermediates, introducing steric hindrance that limits their integration into the hydrogen-bond network of interfacial water (Figure 6e). This modified hydration environment favors Eley–Rideal hydrogenation with water molecules over *H-mediated routes, thereby shifting the dominant reaction pathway. Notably, *H remains highly mobile at the interface, with its hydrogenation barrier largely unaffected by cation coordination, making it a consistent kinetic promoter. Thus, the interplay between cation–intermediate coordination and interfacial water structuring governs the balance between ER and LH pathways, ultimately dictating NO_3RR activity and selectivity (Figure 6f). This ion–water–species coupling serves as a general mechanistic lever applicable to a broad range of electrochemical hydrogenation reactions. For instance, a recent study demonstrated that embedding nitrite-adsorbing ion carriers into Cu/CNT-based charged membranes enriches local NO_2^- near catalytic sites, thereby accelerating its hydrogenation to NH_3 [42]. This strategy achieves a nitrate conversion rate of 94.6% and an ammonia selectivity of 91.9% within only 6 s, while suppressing nitrite accumulation to ~1% (Figure 6g). Importantly, the cooperative adsorption component steers local microenvironments and reaction selectivity without altering the intrinsic catalytic centers, offering a scalable, noble-metal-free route for treating realistic low-concentration nitrate streams.

Designing effective interfaces under realistic electrochemical conditions requires precise control over lattice matching, domain connectivity, and defect distribution to sustain cooperative effects. In practice, however, these structural characteristics rarely exist in isolation. Defect formation, lattice strain, facet exposure, and interfacial coupling often coexist within a single catalyst, and their intertwined impacts collectively dictate the overall NO_3RR performance. For instance, oxygen vacancies can synergize with lattice strain to modulate the binding energies of *NO_2 and *NO, while specific facet orientations stabilize these intermediates and interfacial electronic redistribution further accelerates hydrogenation steps. Such cooperative effects reshape adsorption energetics, intermediate evolution, and HER suppression in a manner far more complex than the sum of individual contributions. Integrating high-resolution microscopy with time-resolved spectroscopy provides critical correlations between interfacial structure, charge/ion transport, and intermediate binding, thereby offering mechanistic insights that guide the rational design of multidimensional catalytic architectures with enhanced activity, selectivity, and durability in NO_3RR.

4. Atomic Dispersed Catalysts for NO_3RR

The electrocatalytic NO_3RR proceeds through a cascade of deoxygenation steps in which nitrate ions (NO_3^-) are sequentially reduced via multiple transient intermediates. Each intermediate possesses distinct adsorption energetics, electronic structures, and reaction kinetics, collectively determining catalytic efficiency and product selectivity. This process is complicated by competing side reactions—most notably the HER—which consumes active hydrogen (*H) species and diverts electrons from nitrate reduction, thereby lowering the FE for NH_3 formation [119–122]. Achieving precise atomic-level control over catalytic sites is therefore essential for directing reaction pathways toward NH_3 production. Atomically dispersed catalysts, with their uniform coordination environments and maximal atomic utilization, provide an ideal platform for such control. Recent studies demonstrate that tailored atomic configurations can modulate intermediate binding energies, suppress HER, and improve selectivity toward NH_3.

4.1. Coordination Engineering

In atomically dispersed catalysts, the coordination environment of the active center critically determines its electronic configuration, charge distribution, and catalytic performance. Subtle variations in coordination geometry modulate orbital hybridization and bond strength, thereby shaping activity, selectivity, and stability. Single-atom catalysts (SACs), with their well-defined atomic structures, provide an ideal platform to investigate these effects [123–126]. Two main strategies have been widely adopted: coordination number modulation and coordinating atom engineering. Lower coordination numbers generally enhance electron localization and strengthen interactions with key intermediates such as *NO_2 and *NO, facilitating their hydrogenation, whereas higher coordination numbers improve structural stability during long-term operation [127–130]. In parallel, tailoring the nature of coordinating atoms—such as N, O, S, or P—alters electronic properties through electronegativity and orbital interactions, thereby tuning intermediate adsorption energies and favoring the NH_3 pathway over HER or N_2 formation [131–133]. Representative examples include Cu–N_3 sites with unsaturated

coordination that lower the Gibbs free energy barrier for NO_3RR [134], Fe–N_4 motifs that provide robust anchoring and electronic tunability [135–143], and asymmetric Ru–Cu dual-atom configurations that exploit charge redistribution to promote cooperative activation of intermediates [135]. These cases highlight the potential of coordination engineering to achieve highly active and durable NO_3RR electrocatalysts.

A central strategy in catalyst design is coordination engineering, wherein the environment surrounding the active center is tuned to control its electronic configuration, charge distribution, and catalytic behavior. Subtle variations in coordination geometry modulate orbital hybridization, bond strength, and the local electronic structure, thereby influencing activity, selectivity, and stability. SACs provide an ideal platform for probing coordination effects owing to their precisely defined structures. Two widely adopted approaches are coordination number modulation and coordinating atom engineering. Reducing the number of ligating atoms typically increases unsaturation, enhances electron localization, and strengthens interactions with key NO_3RR intermediates such as $*NO_2$ and *NO, thereby facilitating their hydrogenation. For example, DFT calculations reveal that Cu–N_3 sites with unsaturated coordination exhibit a lower Gibbs free energy than Cu–N_4 sites, rendering them more favorable for NO_3RR (Figure 7a) [134].

Coordination symmetry breaking fundamentally alters the local electronic environment of the active center by introducing anisotropic ligand fields, which generate uneven charge distribution, modify orbital overlap, and create site-specific reactivity. These perturbations can shift the d-band center and tune adsorption energies in ways that break scaling relations between reaction intermediates, enabling more independent control over key hydrogenation and coupling steps (Figure 7b). A common approach involves incorporating heteroatoms such as oxygen or sulfur alongside nitrogen to form asymmetric ligand fields that polarize the active center. This modification adjusts the d-band structure and intermediate interactions, as illustrated by RuN_2-CuN_3 sites [135]. The differential charge densities of RuN_4/C, CuN_4/C, and RuN_2CuN_3/C were calculated to elucidate the electrical properties of Ru and Cu sites and to study the synergistic interactions of the two asymmetric coordination metal atoms as well. Through the asymmetric deployment of the modulated RuN_2-CuN_3, the surface charge distribution appears significantly polarized (Figure 7c). Electron enrichment near RuN_2 and electron deficiency near CuN_3 are possibly attributed to the electron transfer from the Cu site to the Ru site. The modulated RuN_2-CuN_3 has a strong synergistic effect, the *4d* orbital of Ru is closer to the Fermi level, and it has a stronger adsorption effect for the reaction intermediates (Figure 7d).

Heteroatom doping engineering is a prominent regulatory strategy for atomic-level catalysts, offering significant advantages in catalyst systems. This approach serves a dual function in optimizing catalytic behavior. First, heteroatoms such as N, P, S, or B reinforce the stability of metal active centers by acting as robust anchoring sites for isolated metal atoms [136–138]. Owing to their distinct electronegativities and electronic configurations, these heteroatoms form strong coordination bonds with metal species, effectively mitigating the migration or aggregation of isolated atoms—an issue that often compromises catalytic durability. Second, heteroatom doping enables precise control over the oxidation state and electronic structure of central metal atoms. Electron transfer between dopants and metal centers, driven by differences in electronegativity and orbital hybridization, redistributes electron density, modulates metal d-orbital energy levels, and alters the strength of interactions with reaction intermediates. Such fine-tuning optimizes adsorption and desorption energies for key intermediates, accelerating RDS while suppressing side reactions. Collectively, these effects—enhanced stability and tailored electronic properties—directly translate into improved catalytic performance. By bridging structural stability with electronic tunability, heteroatom doping engineering emerges as a pivotal method for enhancing both the efficiency and selectivity of catalytic reactions, providing a versatile platform for the rational design of high-performance carbon-based single-atom catalysts [139–143]. Recently, a direct and low-cost planar chlorination engineering strategy was reported, in which C–Cl bonds were introduced in the planar direction of Fe–N_4 catalytic sites supported on N,Cl co-doped carbon (Fe–N_4/CNCl) (Figure 7e) [144]. The introduction of adjacent C–Cl bonds disrupted the geometric symmetry of conventional Fe–N_4 sites, thereby increasing site polarity. Theoretical calculations confirmed that asymmetric Fe–N_4 sites with adjacent C–Cl bonds enhance the adsorption of polar $*NO_2$ intermediates, promoting deep NO_3^- reduction, improving NO_3RR activity toward NH_3, and lowering the energy barrier of the RDS.

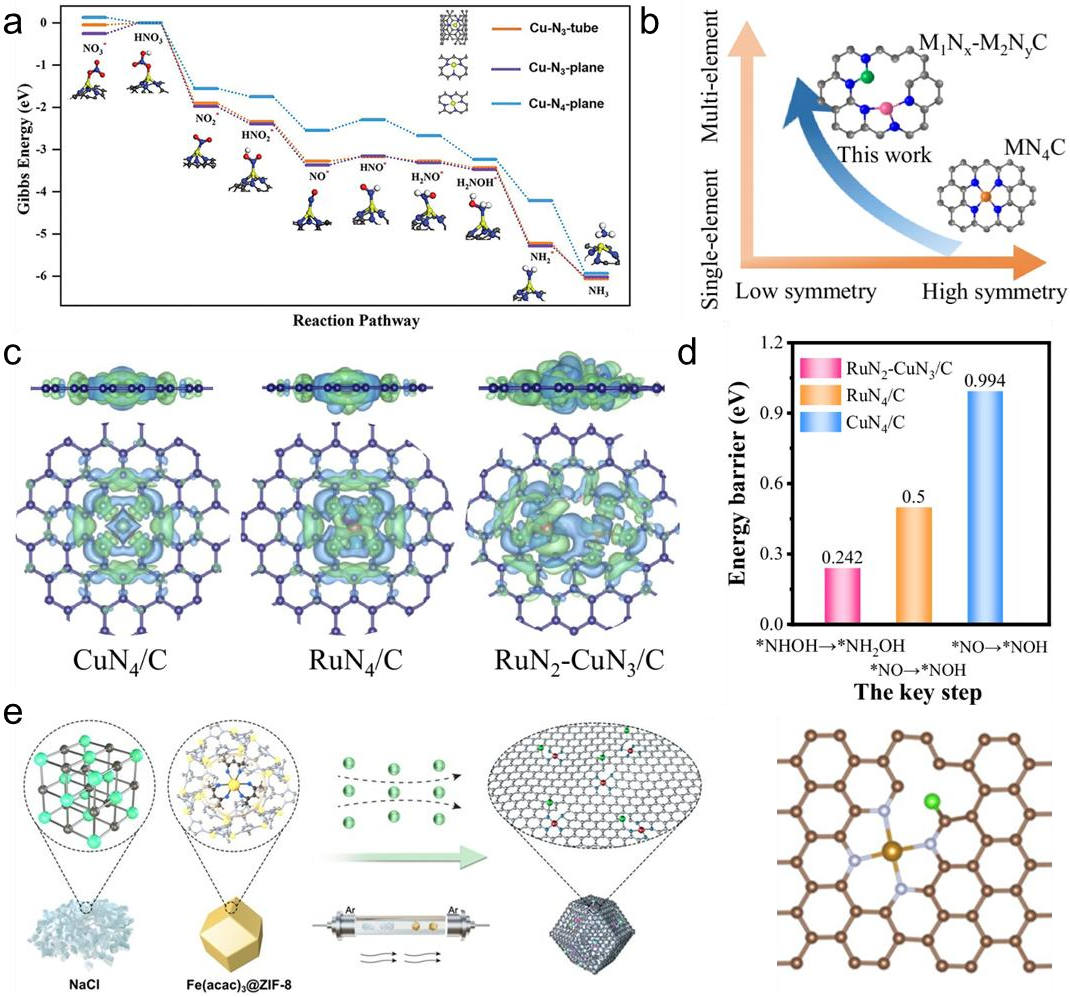

Figure 7. (**a**) Optimal NO_3RR pathway for Cu-N_3–tube (orange line), Cu-N_3–plane (purple line), and Cu-N_4–plane (blue line). (**b**) A research tendency of single atom catalysts to increase the variety of metal elements on the support and form asymmetric coordination structures. (**c**) The differential charge densities of RuN_4/C, CuN_4/C, and RuN_2CuN_3/C. (**d**) The energy barriers of the key steps on RuN_4/C, CuN_4/C, and RuN_2CuN_3/C. Reproduced with permission [135]. Copyright 2025 with permission from Springer Nature. (**e**) Schematic illustration of the synthesis of the Fe–N_4/CNCl catalyst. Reproduced with permission [144]. Copyright 2025 with permission from the American Chemical Society.

4.2. Distance Effect in Atomically Dispersed Catalysts for NO_3RR

In addition to coordination environment engineering, the spatial arrangement of active sites—known as the distance effect—has emerged as a critical structural parameter governing catalytic activity and selectivity [145]. This effect manifests in two principal dimensions: the distribution of isolated single atoms across the catalyst surface and the precise interatomic distances in dual-atom or cluster configurations. Modulating these distances can tune electronic coupling between sites, optimize intermediate migration pathways, and enable cooperative activation in multi-step reduction processes.

Metal–organic frameworks (MOFs) provide an ideal platform to regulate the spatial distribution of active sites, as their well-defined coordination networks and tunable pore structures allow precise control over the distance between single-atom centers. For SACs, the average distance between metal centers determines the degree of electronic isolation. Excessive proximity can induce electronic interactions or partial aggregation, shifting the *d*-band center and diminishing the intrinsic advantages of SACs. Conversely, overly dispersed atoms may reduce the likelihood of multi-site activation, where adjacent active centers facilitate proton-coupled electron transfer (PCET) via spillover or relay mechanisms in NO_3RR. Although direct studies on NO_3RR are limited, analogous evidence from other electrocatalytic systems underscores the importance of distance regulation. For instance, in CO_2RR (Figure 8a), ZnN_4 sites decorated with an axial thiophene-S ligand (near-range regulation) and embedded in a P-doped carbon matrix (long-range regulation) synergistically enhance electron localization, strengthen *COOH adsorption, and achieve nearly 100% FE [146]. Such evidence suggests that combining MOF-derived

spatial control with multi-scale coordination engineering—through both local ligand modulation and long-range atomic environment design—offers a powerful strategy to optimize isolated sites for complex multi-electron processes like NO_3RR, ultimately improving activity, selectivity, and durability.

In electrocatalytic NO_3RR, the spatial arrangement between active metal centers critically influences adsorption strength, intermediate stabilization, and proton–electron transfer pathways [147]. When two active sites are positioned at an optimal sub-nanometer distance, they can cooperatively adsorb and activate nitrate-derived intermediates ($*NO_3$, $*NO_2$, *NO) through a dual-site mechanism. Such proximity facilitates charge redistribution and enhances the local electric field, thereby lowering the activation barrier for N–O bond cleavage and promoting sequential hydrogenation steps toward $*NH_2$ and NH_3. In contrast, excessively distant active sites behave more like isolated single atoms, diminishing cooperative adsorption and potentially limiting reaction rates due to sluggish PCET. A representative example is a Fe–Cu diatomic catalyst anchored on holey nitrogen-doped graphene (Fe/Cu-HNG) [147], in which Fe and Cu atoms are coordinated as $N_2Fe–CuN_2$ dual sites with precisely controlled sub-nanometer spacing (Figure 8b). This configuration enables Fe and Cu to selectively bind and activate different nitrogen-containing intermediates, establishing a synergistic pathway in which Fe centers facilitate $*NO_3/*NO_2$ activation while Cu promotes hydrogenation. As a result, the catalyst achieves a FE of 92.5% at −0.3 V (vs. RHE) and an NH_3 yield rate of 1.08 mmol h^{-1} mg^{-1} at −0.5 V. The DFT calculations confirm that this dual-site arrangement optimizes adsorption energies, suppresses excessive intermediate binding, and smooths the free-energy landscape for the entire NO_3RR cascade—underscoring the critical role of precise interatomic distance control in catalyst design.

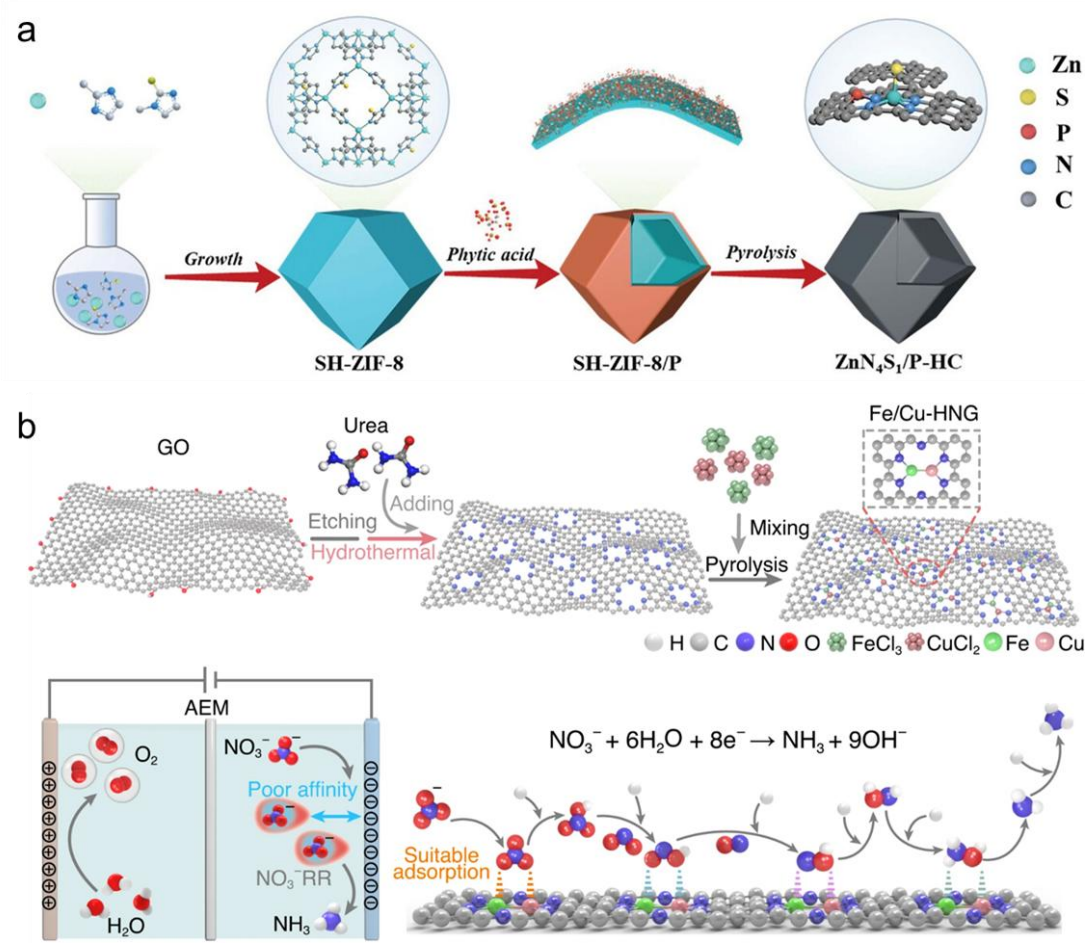

Figure 8. (**a**) Schematic illustration of the synthesis of ZnN_4S_1/P-HC. Reproduced with permission [146]. Copyright 2023 with permission from Wiley-VCH GmbH. (**b**) Schematic illustration of catalyst construction. Electrochemical nitrate reduction and the catalytic conversion steps from NO_3^- to NH_3. Reproduced with permission [147]. Copyright 2023 with permission from Springer Nature.

4.3. Single Atom–Particle Synergy in NO_3RR

The concept of tandem catalysis has recently gained significant attention across various reactions, emerging as a promising strategy to address the challenges of multistep pathways such as the NO_3RR. Tandem catalysts

integrate distinct functional sites within a single system, each tailored to optimize specific elementary steps of the NO_3RR process. This design overcomes a key limitation of single-site catalysts, which often fail to efficiently mediate all reaction stages due to conflicting requirements for intermediate adsorption and activation energies [148,149]. In NO_3RR, tandem architectures can deliver high catalytic activity, selective ammonia production, and elevated FE. Their efficacy arises from the well-coordinated synergistic interplay between two specialized catalytic sites: one is optimized to accelerate the initial reduction of nitrate to nitrite ($NO_3^- \rightarrow NO_2^-$), while the other is fine-tuned for the subsequent conversion of nitrite to ammonia ($NO_2^- \rightarrow NH_3$) [150]. This functional specialization minimizes energy barriers for each step, avoiding kinetic bottlenecks. Beyond stepwise acceleration, the synergy involves atomic-scale interactions—such as modulated interfacial electron transfer, optimized intermediate spillover, and suppression of side reactions—that collectively enhance overall efficiency [151–154].

In NO_3RR, tandem catalysis offers a powerful strategy for addressing the conflicting requirements of multistep pathways. By integrating two functionally distinct active sites within a single catalyst, each optimized for a specific elementary step, it is possible to reduce energy barriers, alleviate adsorption–activation conflicts, and maintain high reaction selectivity. Typically, one site is tailored for the efficient activation of nitrate or nitrite species, while the other promotes subsequent hydrogenation steps toward ammonia. The proximity and interplay of these sites facilitate interfacial electron transfer, hydrogen spillover, and local electric field enhancement, collectively accelerating reaction kinetics and suppressing side reactions. Representative implementations of this principle highlight its broad applicability. In a Janus Cu@Ni tandem catalyst, Cu-rich and Ni-rich domains perform complementary roles in NO_3^-/NO_2^- activation and hydrogenation, delivering enhanced overall efficiency (Figure 9a) [155]. A dual-active-site system comprising sub-nanometric RuO_x clusters supported on palladium metallene leverages hydrogen spillover and hydrogen-bond-mediated interactions to promote sequential reduction steps, optimize intermediate adsorption, and lower activation barriers, achieving outstanding NO_3RR performance under −0.5 V vs. RHE (Figure 9b) [156,157]. Similarly, a Ni_6@CuFe-LDH composite catalyst exhibits strong synergistic coupling between Ni_6 clusters and the CuFe-LDH support (Figure 9c), reaching a FE for NH_3 of 97% and a yield of 0.91 mmol mg^{-1} h^{-1}, markedly surpassing the performance of pristine CuFe-LDH (73%) (Figure 9d) [17]. Together, these examples illustrate how tandem catalyst architectures translate atomic-level synergy into high activity and selectivity in NO_3RR.

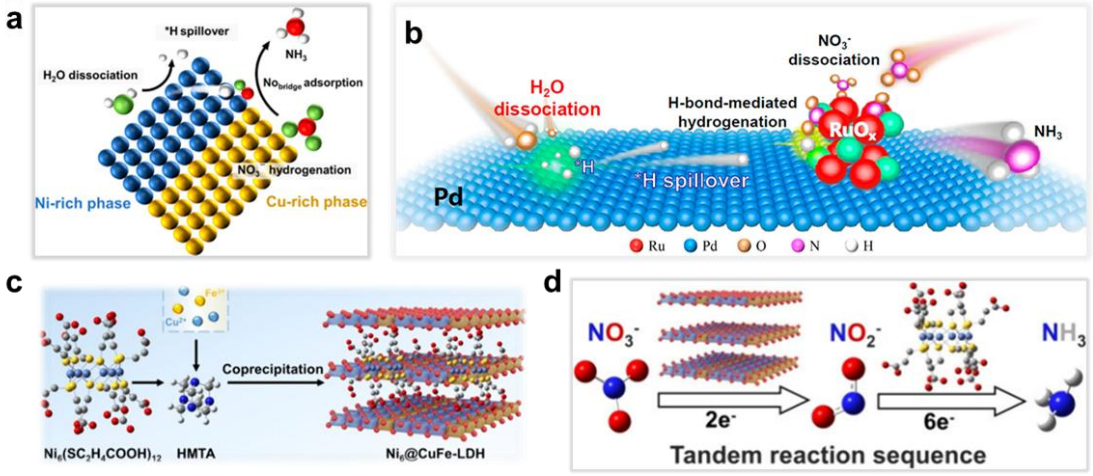

Figure 9. (**a**) The reaction mechanism of the enhanced NO_3RR process over $Cu_{50}Ni_{50}$-Janus/C. Reproduced with permission [155]. Copyright 2024 with permission from the American Chemical Society. (**b**) The reaction mechanism of hydrogen spillover and hydrogen-bond interaction for the RuO_x/Pd catalyzed NO_3RR process. Reproduced with permission [156]. Copyright 2023 with permission from the American Chemical Society. (**c**) Schematic illustration of the preparation procedure of Ni_6@CuFe-LDH composites. (**d**) Tandem Reactions of NO_3RR to Ammonia over Ni_6@CuFe-LDH electrocatalysts. Reproduced with permission [17]. Copyright 2025 with permission from the American Chemical Society.

Bimetallic composites that integrate complementary metal macrocycles can achieve efficient and stable NO_3RR performance across a broad pH range. For instance, a Cu_1Fe_3Pc composite (mass ratio 1:3) prepared via a solvothermal method combines copper phthalocyanine (CuPc) and iron phthalocyanine (FePc) into a dual-site system in which directional electron transfer from CuPc to FePc enriches the latter with electrons, thereby enhancing nitrate adsorption and synergistically improving reaction efficiency [158,159]. Beyond such

macrocyclic systems, diatomic catalysts—particularly heterometallic configurations—can exploit interatomic synergy to regulate electrochemical activity. In one example, frustrated Lewis pair (FLP) motifs composed of spatially proximate Cu and Co single atoms facilitated rapid relay conversion of NO_3^- to NO_2^- and subsequently to NH_3 via complementary Lewis acid–base interactions, demonstrating that FLP chemistry offers an alternative pathway to conventional diatomic synergy [160]. Spatially separated heteroatomic pairs can also enable tandem catalysis. Dual-atom Fe–Mo catalysts featuring MoN_5 and FeN_4 sites catalyze the stepwise reduction of NO_3^- to NO_2^- and NO_2^- to NH_3, respectively, through site-specific activity [161]. In another design, a single-atom Cu-bearing tungsten oxide catalyst (Cu_1/WO_3) delivered high NO_3RR activity by coupling water dissociation on WO_3 with electron-deficient Cu_1 sites for nitrate conversion [162]. Theoretical calculations indicated that WO_3 provides protons to the Cu_1 site, which then efficiently reduces nitrate to ammonia. This dual-driven mechanism breaks the linear scaling limitations typically associated with multi-electron/proton transfer on single-atom catalysts, offering a versatile design principle for next-generation NO_3RR catalysts.

As summarized in Table 1, recent years have witnessed significant progress in both atomically dispersed catalysts and nanocrystalline catalysts for electrocatalytic nitrate reduction to ammonia. These two categories embody complementary design philosophies: atomically dispersed catalysts enable precise tuning of coordination environments and electronic structures at the single-site level, while nanocrystalline catalysts offer abundant low-coordination surface atoms and facet-dependent reactivity. Both have delivered outstanding NO_3RR performance, achieving high NH_3 selectivity, FE, yield, and operational stability. Given the multi-step deoxygenation–hydrogenation sequence of NO_3RR and the unavoidable competition from side reactions such as the HER, tailoring catalyst architectures at the atomic scale remains essential for optimizing reaction pathways and suppressing undesired products.

Table 1. Performance of atomically dispersed and nano catalysts for NO_3RR.

Catalyst	Potential (vs. RHE)	FE (NH_3)	NH_3 Yield Rate	Ref.
O-Cu–PTCDA	−0.4 V	85.9	436 ± 85 μg h^{-1} cm^{-2}	[12]
TTM-CuNP/CNT-EM	—	91.9	—	[42]
Ru3%-HEO	−0.5 V	91.3	5.79 mg h^{-1} mg_{cat}^{-1}	[49]
$Ru_{15}Co_{85}$ HND	+0.4 V	97 ± 5	3.2 mol g_{cat}^{-1} h^{-1}	[52]
$Cu_{50}Ni_{50}$	−0.06 V	58 ± 2%	—	[63]
CuN_3-SACs/NCNT	−0.8 V	89.64	70.8 mol h^{-1} mg_{metal}^{-1}	[134]
Cu_1/WO_3	−0.5 V	93.7	1274.4 mg_N h^{-1} gCu^{-1}	[162]
Cu_4 $(PTI)_4$	−40 mA cm^{-2}	100	2660.63 μg h^{-1} mg^{-1}	[163]
$Ag_1@Cu_2O$ NWs	−0.1 V	>90	—	[164]
Cl-Fe-NC	−0.68 V	99.4	9.397 mg h^{-1} cm^{-2}	[165]
Ru_1-Co/HCO	−0.33 V	100	7.03 mg h^{-1} cm^{-2}	[166]
SAs&NPs/SC	−0.7 V	97.2	4.8 mg h^{-1} cm^{-2}	[167]
NiBDC@HsGDY@Cu	−0.41 V	99.2	0.623 mmol h^{-1} cm^{-2}	[168]
Pd-CuO	−0.5 V	90.0	4.2 mol h^{-1} g_{cat}^{-1}	[169]
FeN_3PO	−0.4 V	90.28	5.85 mg h^{-1} cm^{-2}	[140]
Rh_1-TiO_2	−0.5 V	94.7	29.98 mg h^{-1} mg_{cat}^{-1}	[170]
SnCu-DG	−0.8 V	99.5	75.82 mg h^{-1} mg_{cat}^{-1}	[81]
NiCo-DSAC/Mxene	−0.5 V	92.46	8.46 mg h^{-1} cm^{-2}	[171]
RhNi@Rh BML	0.05 V	98.5	13.4 mg h^{-1} mg_{cat}^{-1}	[172]
Co-OCPaper	−0.8 V	—	3.9 mg h^{-1} cm^{-2}	[173]
Cu-N_4/O_4	−0.7 V	94.7	1.83 mmol h^{-1} mg_{cat}^{-1}	[174]
Co_1-P/NPG	−0.7 V	93.8	8.6 mg h^{-1} mg_{cat}^{-1}	[175]
Co─N─C	−0.5 V	95.5 ± 2.8	20.5 ± 2.7 mg h^{-1} mg_{cat}^{-1}	[176]
FeSAC/FeP@C	−1.0 V	95.6 ± 0.5	36.2 ± 3.1 mg h^{-1} mg_{cat}^{-1}	[177]
Bi_1-$CuCo_2O_4$	−0.8 V	95.53	7.63 mg h^{-1} cm^{-2}	[178]
Fe_1/V_2O_5	−0.7 V	97.1	12.5 mg h^{-1} cm^{-2}	[179]
Sn-FeS_2	−0.5 V	96.7	15.8 mg h^{-1} cm^{-2}	[180]
Fe_1/NC-X	− 0.7 V	86.0	18.8 mg h^{-1} mg_{cat}^{-1}	[181]
Au_xCu	−0.8 V	99.86	6.21 mmol h^{-1} cm^{-2}	[182]
Si/I-NiO@CC	−0.3 V	96.8	10.6 mg h^{-1} cm^{-2}	[16]
ISAA In-Pdene	−0.6 V	87.2	28.06 mg h^{-1} mg_{cat}^{-1}	[183]
CuN_4&Cu_4/NTC	−0.75 V	94.3	88.2 mmol h^{-1} mg_{cat}^{-1}	[184]
RuSACs-CF	−0.55 V	92.3	1.352 mg h^{-1} cm^{-2}	[185]
ZnNC-900-2h	−0.8 V	91	1.2904 mmol h^{-1} cm^{-2}	[186]
CoCu-NC	−0.6 V	95.3	2.41 mg h^{-1} cm^{-2}	[187]

Catalyst	Potential (vs. RHE)	FE (NH_3)	NH_3 Yield Rate	Ref.
PR-CuNC	−0.5 V	94.61	3.74 mg h^{-1} cm^{-2}	[188]
Fe/Cu-HNG	−0.3 V	92.51	1.08 mmol h^{-1} mg_{cat}^{-1}	[189]
Fe-Mo DSAC	−0.78 V	94	13.56 mg h^{-1} cm^{-2}	[161]
Fe_1/MXene	−1.4 V vs. Ag/AgCl	82.9	—	[190]
Cu/Co-CN	−0.6 V	93	7.24 mg h^{-1} mg^{-1}	[160]
CuSA/V-LDH	−0.6 V	95.3	1.78 mg h^{-1} cm^{-2}	[191]
Fe/NHCTs	—	95	9.12 mg h^{-1} cm^{-2}	[192]
FL-Ag/HEA/CNFs	−0.57 V	92.61	2.447 mmol h^{-1} mg_{cat}^{-1}	[193]
Mo-Fe_2O_3	−0.5 V	95	0.494 h^{-1} mg_{cat}^{-1}	[194]
Bi_1Pd	−0.6 V	100	33.8 mg h^{-1} cm^{-2}	[195]
Cu/Ni-NC	−0.7 V	97.28	0.324 mmol h^{-1} cm^{-2}	[196]
PCN-Cu-DAC	−0.77 V	97.8	102 mg h^{-1} cm^{-2}	[197]
CuN_4	−1.1 V	87.2	2.602 mg h^{-1} cm^{-2}	[198]
CoSA-CoNP@CC	−0.6 V	95.6	0.275 mmol h^{-1} cm^{-2}	[199]
PdCu SAA	—	97.1 ± 1.2	0.0154 mol h^{-1} cm^{-2}	[200]
CuN_1O_2	−0.6 V	96.5	3.12 mg h^{-1} cm^{-2}	[201]
NiSA@BNG	−0.4 V	95	0.168 mg h^{-1} cm^{-2}	[202]
CoN_4	−1.1 V	94.4	3.08 mmol h^{-1} cm^{-2}	[202]
d-CoCP-n	−0.5 V	97	0.78 mmol h^{-1} cm^{-2}	[203]
Zr-TiON	−60 mA cm^{-2}	94.8	11.94 mg h^{-1} mg_{cat}^{-1}	[204]
Cu_2/N_3-6	−0.8 V	97.4	18.2 mg h^{-1} cm^{-2}	[205]
Ag_1/ NOCNT	−0.5 V	97.9	2.8 mmol h^{-1} mg_{cat}^{-1}	[206]
RuCu DACs/NGA	−0.5 V	95.7	3.1 mg h^{-1} cm^{-2}	[207]
NiFe-LDH-O_v	—	97.2	—	[208]

Note: In the table above, the potential is all versus reversible hydrogen electrode (vs. RHE). Where other special units or cases exist, they are marked separately.

5. Advanced Technology for NO_3RR

In electrocatalytic NO_3RR, the multiplicity of intermediates and the presence of competing side reactions present major challenges for mechanistic understanding. Advanced techniques have therefore become indispensable, with *in situ* and *operando* characterization enabling continuous, real-time monitoring of catalyst structure and surface chemistry under operating conditions. By coupling electrochemical control with spectroscopic or diffraction-based methods, these approaches capture transient events in intermediate formation, transformation, and decay, directly correlating structural evolution with catalytic performance. Complementarily, density functional theory (DFT) and related computational modeling provide atomistic insights into adsorption configurations, energy landscapes, and reaction pathways, offering a powerful framework to validate experimental observations and uncover hidden mechanisms. The integration of experimental characterization with theoretical calculations thus establishes a holistic toolkit for elucidating the complex reaction network of NO_3RR.

In situ differential electrochemical mass spectrometry (DEMS) integrates electrochemical control with mass spectrometric analysis, enabling real-time detection of volatile and vaporizable products—including gas molecules and small organic compounds—formed during electrolysis or electrocatalysis [208,209]. By monitoring characteristic mass-to-charge (m/z) signals, DEMS achieves precise identification of reaction products, providing direct experimental evidence for elucidating reaction pathways and capturing transient intermediates. This capability has been widely applied in areas such as organic electrosynthesis and energy catalysis. Similarly, *in situ* Fourier transform infrared spectroscopy (FTIR) combines infrared spectroscopic analysis with *in situ* measurement to dynamically record spectral changes under actual reaction or adsorption/desorption conditions [77]. The technique directly reveals variations in molecular structure, functional groups, and chemical states, offering insight into the chemical transformations occurring at the catalyst surface. *In situ* Raman spectroscopy operates on a comparable principle, coupling Raman scattering with *in situ* monitoring to track structural, compositional, and phase changes in real time [210]. For atomic-scale insights, the XAS is one of the few methods capable of probing the local electronic and geometric structure of specific elements [211–215]. It relies on the absorption of X-ray by matter, with analysis of the resulting spectra—particularly the X-ray absorption near-edge structure (XANES) and extended X-ray absorption fine structure (EXAFS)—revealing oxidation states, coordination numbers, and the identity of neighboring atoms. When integrated into an *in situ* setup, XAS enables real-time monitoring of these structural parameters, thus linking dynamic electronic and atomic rearrangements to catalytic function.

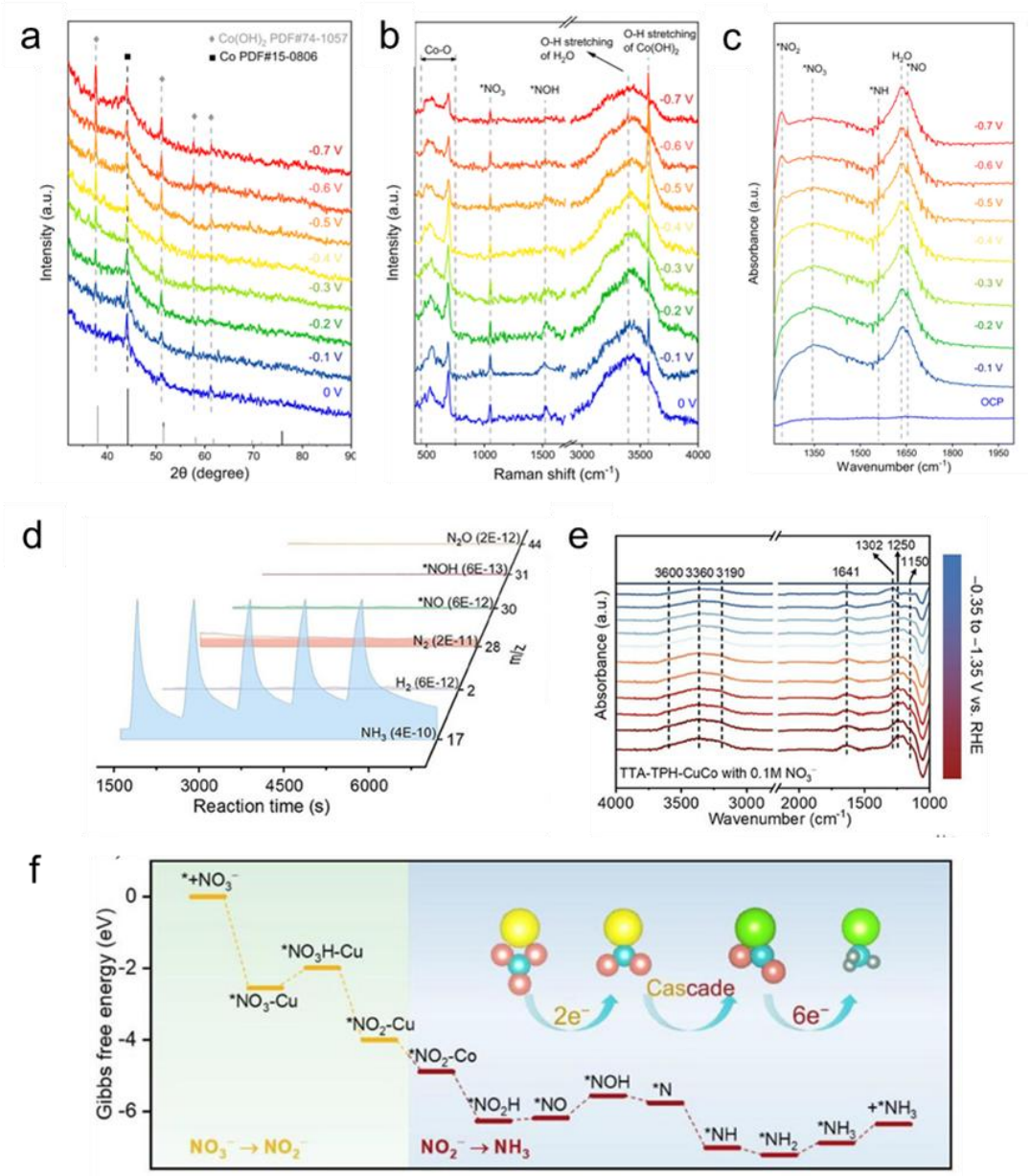

Figure 10. (**a**) *In situ* electrochemical XRD patterns of the Cr-CoO_x electrocatalyst. Reproduced with permission [216]. Copyright 2025 with permission from The Royal Society of Chemistry. (**b**) *In situ* electrochemical Raman spectra of the Cr-CoO_x electrocatalyst. (**c**) *In situ* ATR-FTIR spectra of the Cr-CoO_x electrocatalyst at different applied potentials. Reproduced with permission [77]. Copyright 2023 with permission from The Royal Society of Chemistry. (**d**) *In situ* DEMS patterns of TTA-TPH-CuCo. (**e**) *In situ* ATR-IRAS measurements under different potentials for TTA-TPH-CuCo. Reproduced with permission [217]. Copyright 2025 with permission from Wiley-VCH GmbH. (**f**) Free energies of the NO_3RR reaction pathway at Cu and Co. Reproduced with permission [65]. Copyright 2024 with permission from Wiley-VCH GmbH.

Validating an entire catalytic reaction pathway typically requires the integration of multiple *in situ* characterization techniques with theoretical calculations to achieve synergistic verification. For example, Lv and co-workers designed a Cr-doped Co-based catalyst and systematically investigated its reaction pathway through a suite of *in situ* techniques. *In situ* X-ray diffraction (XRD) revealed the disruption of the crystalline phase structure (Figure 10a), while DFT calculations corroborated the dynamic reconstruction mechanism [216]. Concurrently, *in situ* electrochemical Raman spectroscopy and *in situ* attenuated total reflection Fourier transform infrared spectroscopy (ATR-FTIR) identified reaction intermediates (Figure 10b,c), providing direct evidence for the NO_3RR-to-NH_3 mechanism [77]. The results demonstrated that interfacial water participates in the electrocatalytic process, and strong hydrogen-bond interactions between the Cr-doped $Co(OH)_2$ surface and interfacial H_2O facilitate water dissociation to generate active hydrogen (*H), which in turn accelerates the NO_3RR pathway at metallic Co sites [71]. Similarly, Zhang et al. employed *in situ* DEMS (Figure 10d) and *in situ* attenuated total

reflection surface-enhanced infrared absorption spectroscopy (ATR-IRAS, Figure 10e) to detect reaction-generated intermediates and adsorbed species on the TTA-TPH-CuCo surface [217]. Characteristic signals of key intermediates (*NOH and *NH_2) revealed that nitrate conversion to ammonia proceeds via the pathway shown in Figure 10f [65]. Integrating these experimental observations with DFT calculations enabled the elucidation of a tandem catalytic mechanism: Cu sites serve as activation centers for reactant adsorption and the initial two-electron transfer steps, while the –N–Co–O– interface facilitates water adsorption and dissociation, generating a *H-rich microenvironment that drives subsequent six-electron transfer reactions, ultimately enhancing ammonia synthesis efficiency. To clarify the NO_3RR-to-NH_3 pathway over Ni_6@CuFe-LDH and CuFe-LDH, Li and co-workers used *in situ* Raman spectroscopy (Figure 11a) and FTIR spectroscopy (Figure 11b) to track surface species evolution from 0 to −0.5 V vs. RHE [156]. Combined with DFT analysis, they identified a shift in RDS from NH_3 desorption to the *NO_3 → *NO_2 conversion step. Furthermore, Jiang and co-workers applied *in situ* XAS (Figure 11c), to capture the dynamic structural evolution of Mn active sites during reaction [218]. Integrating *in situ* spectroscopy with DFT simulations, they clarified the formation pathways of intermediates and explained the origin of the catalyst's high activity. Likewise, Wu and collaborators resolved the dynamic reconstruction of atomically dispersed Cu–N_3 sites during CO_2 reduction using *in situ* XAS in combination with other *in situ* techniques (Figure 11d) [219].

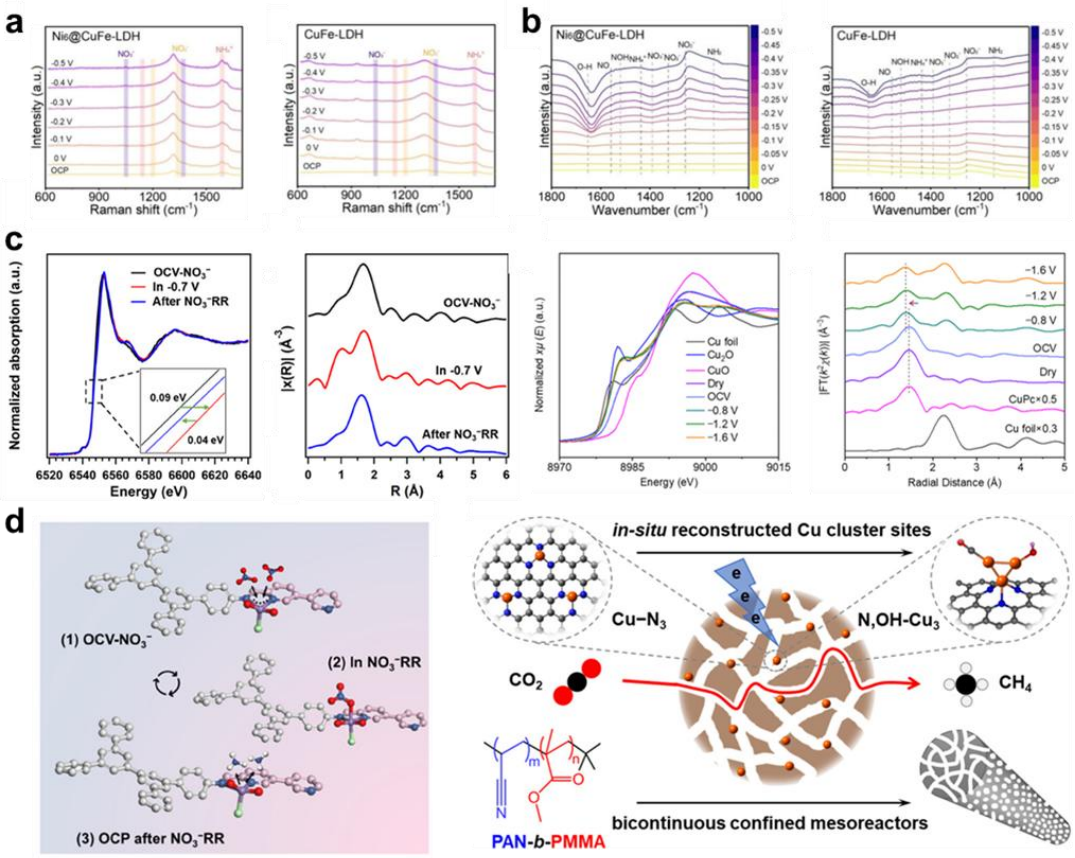

Figure 11. (**a**) *In situ* Raman spectra of Ni_6@CuFe-LDH and CuFe-LDH. (**b**) *In situ* FTIR spectra of Ni_6@CuFe-LDH and CuFe-LDH. Reproduced with permission [156]. Copyright 2023 with permission from American Chemical Society. (**c**) Mn K-edge XANES and EXAFS of ImPy-COF-Mn under various *in situ* XAS conditions. Cu K-edge XANES and EXAFS of the Cu–N/IPCF. Reproduced with permission [218]. Copyright 2025 with permission from Wiley-VCH GmbH. (**d**) The dynamic reconstruction under realistic CO_2 reduction conditions. Reproduced with permission [219]. Copyright 2024 with permission from the American Chemical Society.

Theoretical modeling, particularly DFT, has become an indispensable complement to experimental research in electrocatalytic nitrate reduction. By mapping adsorption geometries, reaction energetics, and elementary steps at the atomic scale, DFT enables the identification of active sites, rate-determining steps, and competing pathways that are often inaccessible to *in situ* characterization. Recent advances further integrate machine learning algorithms and high-throughput computational screening into the DFT framework, significantly accelerating catalyst discovery. Machine learning models trained on large DFT datasets can rapidly predict adsorption energies

and activity descriptors across vast chemical spaces, while high-throughput workflows allow systematic exploration of diverse compositions, coordination environments, and surface terminations. Together, these approaches provide a powerful platform for uncovering structure–property relationships, guiding rational catalyst design, and proposing new material candidates for NO_3RR with enhanced activity and selectivity. As such, the synergy between DFT, machine learning, and data-driven screening is emerging as a frontier for advancing both mechanistic understanding and practical catalyst development in nitrate electroreduction.

DFT calculations serve as a theoretical compass for experimental design by providing atomistic insights into adsorption configurations, reaction energetics, and potential-dependent free energy landscapes of NO_3RR. Such simulations not only identify the thermodynamically favorable pathways and rate-determining steps but also clarify how coordination environments, defect structures, and electronic states influence intermediate stabilization. A pioneering strategy was proposed to enhance NO_3RR-to-NH_3 electrosynthesis by introducing f–d–p gradient orbital coupling in electrocatalysts to circumvent the scaling relationship between adsorption strengths of different intermediates (Figure 12a) [110]. Theoretical calculations revealed that gradient orbital coupling in Co_3O_4 induces lattice strain that tunes the adsorption of key intermediates (*H and *NO) in opposite directions. Guided by this insight, Ce-doped Co_3O_4 was synthesized experimentally, exhibiting superior electrochemical performance for nitrate-to-ammonia conversion.

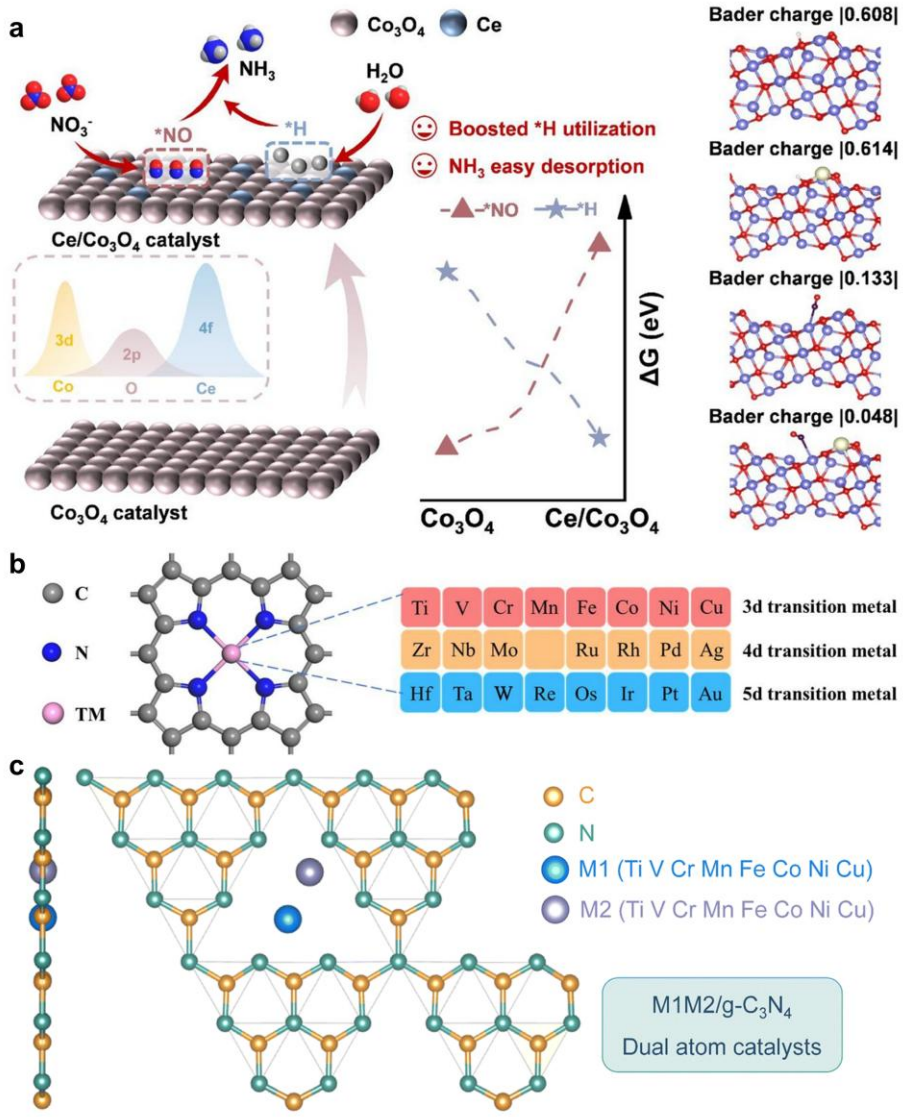

Figure 12. (**a**) Schematic illustration of f–d–p gradient orbital coupling on the cobalt catalyst for NH_3 electrosynthesis. Reproduced with permission [110]. Copyright 2025 with permission from Wiley-VCH GmbH. (**b**) The structure of two-dimensional metalloporphyrin monolayers. Reproduced with permission [220]. Copyright 2024 with permission from Elsevier B.V. (**c**) The optimized M_1M_2/g-C_3N_4 structure is used to deal with NO_3RR. Reproduced with permission [221]. Copyright 2024 with permission from The Royal Society of Chemistry.

Advanced high-throughput screening and machine learning offer powerful means to identify promising NO_3RR catalysts while reducing trial-and-error inefficiencies. High-throughput frameworks rapidly evaluate diverse compositions and coordination motifs, generating large datasets of adsorption energies, charge-transfer characteristics, and reaction barriers. These datasets underpin machine learning models that capture hidden correlations between structural parameters and catalytic performance, enabling low-cost prediction of activity and selectivity trends across vast chemical spaces. This integrated strategy accelerates catalyst discovery, conserves resources, and provides a data-driven pathway for rational NO_3RR design. For instance, mechanistic studies revealed that several catalysts preferentially follow the *N → *NOH → *N → *NH route to NH_3 while suppressing HER and byproducts. Machine learning further established strong correlations between nitrate adsorption free energy and intrinsic descriptors, while PDOS and COHP analyses confirmed strong d–p orbital interactions driving nitrate activation. Together, these approaches not only identified efficient single-atom catalysts but also established design principles for ammonia production with broad implications for environmental remediation and sustainable energy conversion (Figure 12b) [220]. High-throughput screening based on first-principles calculations further demonstrated that g-C_3N_4–supported dual-atom catalysts (M_1M_2/g-C_3N_4, M_1 = M_2 = Ti, V, Cr, Mn, Fe, Co, Ni, Cu) exhibit remarkable catalytic potential for NO_3RR. Multilevel descriptors were employed to elucidate the origins of activity, enabling rapid identification of promising candidates. Among the 36 M_1M_2/g-C_3N_4 configurations evaluated, TiFe/g-C_3N_4 showed the most favorable performance, with a limiting potential of −0.21 eV (Figure 12c) [221].

In summary, *in situ* characterization techniques constitute indispensable, multi-dimensional tools for investigating electrocatalytic nitrate-to-ammonia conversion. These methods are highly effective in revealing dynamic, atomic-scale structural changes in electrocatalysts under realistic operating conditions, including subtle variations in active sites, coordination environments, and phase states during the reaction. They also enable precise monitoring of the transient formation, transformation, and decay of key reaction intermediates—processes that are essential for constructing complete reaction pathways. Moreover, *in situ* characterizations facilitate quantitative assessment of NO_3RR kinetics, encompassing reaction rates, electron-transfer efficiencies, and activation energy barriers. Complementing these experimental capabilities, DFT and other computational modeling approaches provide atomistic perspectives on adsorption configurations, energy landscapes, and elementary reaction steps, thereby validating experimental observations and predicting hidden pathways that are difficult to capture experimentally. The integration of *in situ*/*operando* techniques with theoretical calculations thus offers unparalleled insights into intrinsic catalytic mechanisms, providing a robust foundation for the rational design of electrocatalysts with superior activity and selectivity, as well as for advancing the practical implementation of nitrate reduction technologies. Real-time monitoring of NO_3RR through these approaches, when combined with predictive modeling, further deepens mechanistic understanding and guides the development of highly efficient catalysts. Nevertheless, both experimental and theoretical methodologies face inherent challenges, including the need for complex operational adjustments, high instrumentation costs, and potential discrepancies between modeled and actual reaction conditions. Consequently, the advancement of *operando* techniques and multiscale computational methods that more closely replicate true reaction environments remains a critical research priority.

6. Conclusions

From the comparative analysis of nanocrystalline and atomically dispersed catalysts presented in this work, a clear design logic for high-performance NO_3RR systems emerges. Nanocrystalline catalysts regulate activity and selectivity primarily through facet engineering, size effects, strain modulation, and defect engineering, thereby tuning the adsorption energies of *NO_3, *NO_2, and *NH_x intermediates at the ensemble scale. In contrast, atomically dispersed catalysts offer precision control at the single-site level via coordination-number modulation, heteroatom-induced symmetry breaking, inter-site distance engineering, and single–atom–nanoparticle synergy—directly shaping the local electronic structure and adsorption configuration of intermediates. Despite their structural differences, both classes converge on common mechanistic principles: balancing *NO_2 activation with *H delivery, avoiding over-stabilization of *NO, and suppressing competing HER. This unified mechanistic understanding not only rationalizes the diverse strategies reported in recent literature but also provides a coherent framework for designing next-generation NO_3RR catalysts.

Building on this framework, this review has systematically summarized mechanistic insights, *in situ* characterization methodologies, synthesis approaches, and atomic-scale design strategies for nitrate reduction electrocatalysts. Looking ahead, several research directions warrant priority. First, achieving a deeper and more systematic understanding of structure–activity relationships is essential, linking atomic-level structural features to catalytic performance. This will require integrating advanced *operando* characterization with high-accuracy

theoretical calculations to elucidate intrinsic reaction mechanisms—including reactant activation pathways, adsorption/desorption dynamics of key intermediates, and kinetic characteristics of RDS. Such insights will clarify how specific structural attributes—coordination environment, electronic state, and defect distribution—govern catalytic activity and selectivity, thereby establishing a robust theoretical basis for rational design. Second, novel catalyst architectures should be developed, such as multi-active-site systems that synergistically promote water dissociation, nitrate adsorption, and hydrogenation while suppressing hydrogen evolution; as well as employing coordination regulation, heteroatom doping, and defect engineering to fine-tune electronic structures and surface properties for enhanced intermediate conversion. Third, long-term stability must be addressed by selecting robust supports, optimizing catalyst–support interactions, and engineering corrosion-resistant, anti-agglomeration architectures to sustain activity under prolonged operation. Finally, optimizing the reaction environment—including electrolyte formulation and reactor design—will be critical for translating laboratory-scale advances into industrially viable NO_3RR technologies, thereby advancing sustainable energy conversion and environmental remediation.

Funding

This work was supported by the National Natural Science Foundation of China (No. 22375019) and the Postdoctoral Fellowship Program of CPSF (No. GZC20252673).

Institutional Review Board Statement

Not applicable.

Informed Consent Statement

Not applicable.

Data Availability Statement

Not applicable.

Conflicts of Interest

The authors declare no conflict of interest.

References

1. Kitano, M.; Inoue, Y.; Yamazaki, Y.; et al. Ammonia synthesis using a stable electride as an electron donor and reversible hydrogen store. *Nat. Chem.* **2012**, *4*, 934–940.
2. Ham, C.; Koper, M.; Hetterscheid, D. Challenges in reduction of dinitrogen by proton and electron transfer. *Chem. Soc. Rev.* **2014**, *43*, 5183–5191.
3. Fryzuk, M. Ammonia transformed. *Nature* **2004**, *427*, 498–499.
4. Guo, J.; Chen, P. Catalyst: NH_3 as an Energy Carrier. *Chem* **2017**, *3*, 709–712.
5. Zhang, G.; Li, B.; Shi, Y.; et al. Ammonia recovery from nitrate-rich wastewater using a membrane-free electrochemical system. *Nat. Sustain.* **2024**, *7*, 1251–1263.
6. Kandemir, T.; Schuster, M.; Senyshyn, A.; et al. The Haber–Bosch process revisited: On the real structure and stability of "ammonia iron" under working condition. *Angew. Chem. Int. Ed.* **2013**, *52*, 12723–12726.
7. Talib, S.H.; Ali, B.; Dar, A.H.; et al. Catalytic reduction of N_2O by CO molecules using transition metal-phosphomolybdic acid (TM_1/PMA) single-atom catalysts: A theoretical perspective. *Nano Res. Energy* **2025**, *4*, e9120158.
8. Licht, S.; Cui, B.; Wang, B.; et al. Retracted: Ammonia synthesis by N_2 and steam electrolysis in molten hydroxide suspensions of nanoscale Fe_2O_3. *Science* **2014**, *345*, 637–640.
9. Chen, S.; Perathoner, S.; Ampelli, C.; et al. Electrocatalytic synthesis of ammonia at room temperature and atmospheric pressure from water and nitrogen on a carbon-nanotube-based electrocatalyst. *Angew. Chem. Int. Ed.* **2017**, *129*, 2743–2747.
10. Yu, X.; Han, P.; Wei, Z.; et al. Boron-doped graphene for electrocatalytic N_2 reduction. *Joule* **2018**, *2*, 1610–1622.
11. Qin, S.; Li, K.; Cao, M.; et al. Fe-Co-Ni ternary single-atom electrocatalyst and stable quasi-solid-electrolyte enabling high-efficiency zinc-air batteries. *Nano Res. Energy* **2024**, *3*, e9120122.
12. Chen, G.; Yuan, Y.; Jiang, H.; et al. Electrochemical reduction of nitrate to ammonia via direct eight-electron transfer using a copper–molecular solid catalyst. *Nat. Energy* **2020**, *5*, 605–613.

13. Yang, J.; Qi, H.; Li, A.; et al. Potential-driven restructuring of Cu single atoms to nanoparticles for boosting the electrochemical reduction of nitrate to ammonia. *J. Am. Chem. Soc.* **2022**, *144*, 12062–12071.
14. Jiang, Z.; Wang, Y.; Lin, Z.; et al. Molecular electrocatalysts for rapid and selective reduction of nitrogenous waste to ammonia. *Energy Environ. Sci.* **2023**, *16*, 2239–2246.
15. Wang, Y.-R.; Ding, H.-M.; Yue, M.; et al. Subtle tuning of micro-environment in COFs nanoribbons actuates low electricity-consumption photo-assisted Co-electrolysis of methanol and CO_2. *Nano Res. Energy* **2025**, *4*, e9120146.
16. Feng, C.; Bo, K.; Wan, J.; et al. Triple synergy engineering via metal-free dual-atom incorporation for self-sustaining acidic ammonia electrosynthesis. *Angew. Chem. Int. Ed.* **2025**, *64*, e202505211.
17. Gu, X.; Zhang, J.; Guo, S.; et al. Tiara Ni Clusters for Electrocatalytic Nitrate Reduction to Ammonia with 97% Faradaic Efficiency. *J. Am. Chem. Soc.* **2025**, *147*, 22785–22795.
18. Foster, S.; Bakovic, S.; Duda, R.; et al. Catalysts for nitrogen reduction to ammonia. *Nat. Catal.* **2018**, *1*, 490–500.
19. Liu, Y.; Li, Y.; Sun, J.; et al. Present and future of functionalized Cu current collectors for stabilizing lithium metal anodes. *Nano Res. Energy* **2023**, *2*, e9120048.
20. Zhao, Q.; Gan, R.; Ran, Y.-L.; et al. Single-atom catalysts: Controlled synthesis and dynamic mechanism in electrochemical oxygen evolution substitution reactions. *Rare Met.* **2024**, *43*, 4903–4920.
21. Legare, M.; Belanger-Chabot, G.; Dewhurst, R.; et al. Nitrogen fixation and reduction at boron. *Science* **2018**, *359*, 896–900.
22. Suryanto, B.; Du, H.; Wang, D.; et al. Challenges and prospects in the catalysis of electroreduction of nitrogen to ammonia. *Nat. Catal.* **2019**, *2*, 290–296.
23. Cai, X.; Wang, S.; Peng, L.-M. Recent progress of photodetector based on carbon nanotube film and application in optoelectronic integration. *Nano Res. Energy* **2023**, *2*, e9120058.
24. Yan, J.; Ye, F.; Dai, Q.; et al. Recent progress in carbon-based electrochemical catalysts: From structure design to potential applications. *Nano Res. Energy* **2023**, *2*, e9120047.
25. Sun, R.; Xu, F.; Wang, C.-H.; et al. Rational design of metal selenides nanomaterials for alkali metal ion (Li^+/Na^+/K^+) batteries: Current status and perspectives. *Rare Met.* **2024**, *43*, 1906–1931.
26. Pham, H.Q.; Pham, H.T.Q.; Huynh, Q.; et al. Single-Atom Iridium-Based Catalysts: Synthesis Strategies and Electro(Photo)-Catalytic Applications for Renewable Energy Conversion and Storage. *Coord. Chem. Rev.* **2023**, *486*, 215143.
27. Langevelde, P.; Katsounaros, I.; Koper, M. Electrocatalytic nitrate reduction for sustainable ammonia production. *Joule* **2021**, *5*, 290–294.
28. Bhatnagar, A.; Sillanpää, M. A review of emerging adsorbents for nitrate removal from water. *Chem. Eng. J.* **2011**, *168*, 493–504.
29. Pham, H.Q.; Huynh, T.T. Applications of doped-MXene-based materials for electrochemical energy storage. *Coord. Chem. Rev.* **2024**, *517*, 216039.
30. Gruber, N.; Galloway, J. An earth-system perspective of the global nitrogen cycle. *Nature* **2008**, *451*, 293–296.
31. Zhao, R.; Yan, Q.; Yu, L.; et al. A Bi-Co corridor construction effectively improving the selectivity of electrocatalytic nitrate reduction toward ammonia by nearly 100%. *Adv. Mater.* **2023**, *35*, 2306633.
32. Rosca, V.; Duca, M.; Groot, M.; et al. Nitrogen cycle electrocatalysis. *Chem. Rev.* **2009**, *109*, 2209–2244.
33. Li, J.; Zhan, G.; Yang, J.; et al. Efficient ammonia electrosynthesis from nitrate on strained ruthenium nanoclusters. *J. Am. Chem. Soc.* **2020**, *142*, 15, 7036–7046.
34. Aslam, M.K.; Hussain, I.; Al-Marzouqi, A.H.; et al. Advances in covalent organic frameworks for photocatalytic CO_2 reduction: Strategies and future perspectives. *Nano Res. Energy* **2025**, *4*, e9120149.
35. Liu, X.; Liu, C.; He, X.; et al. Fe-doped Co_3O_4 nanowire strutted 3D pinewood-derived carbon: A highly selective electrocatalyst for ammonia production via nitrate reduction. *Nano Res.* **2024**, *17*, 2276–2282.
36. Zhou, X.; Yang, T.; Li, T.; et al. *In-situ* fabrication of carbon compound NiFeMo-P anchored on nickel foam as bi-functional catalyst for boosting overall water splitting. *Nano Res. Energy* **2023**, *2*, e9120086.
37. Pham, H.Q.; Dao, T.-B.-N.; Nguyen, A.Q.K.; et al. Nitrogen-doped, properties and applications for electrochemical hydrogen production. *Adv. Colloid Interface Sci.* **2025**, *341*, 103493.
38. Li, N.-P.; Zhang, L.; Zhang, H.; et al. Synergistic effect between Er-doped MoS_2 nanosheets and interfacial Mo–N coupling phases for enhanced electrocatalytic hydrogen evolution. *Rare Met.* **2024**, *43*, 1301–1308.
39. Zhang, W.-T.; Wang, X.-Q.; Zhang, F.-Q.; et al. Frontiers in high entropy alloys and high entropy functional materials. *Rare Met.* **2024**, *43*, 4639–4776.
40. Qiao, B.; Wang, A.; Yang, X.; et al. Single-atom catalysis of CO oxidation using Pt_1/FeO_x. *Nat. Chem.* **2011**, *3*, 634–641.
41. Zhang, Y.-Z.; Ao, H.-S.; Dong, Q.; et al. Electrolytes additives for Zn metal anodes: Regulation mechanism and current perspectives. *Rare Met.* **2024**, *43*, 4162–4197.

42. Fan, Y.; Yan, Y.; Nwokonkwo, O.; et al. Tuning nitrate reduction reaction selectivity via selective adsorption in electrified membranes. *Nat. Chem. Eng.* **2025**, *2*, 379–390.
43. Chen, Z.; Zhang, X.; Liu, W.; et al. Amination strategy to boost the CO_2 electroreduction current density of M–N/C single-atom catalysts to the industrial application level. *Energy Environ. Sci.* **2021**, *14*, 2349–2356.
44. Liu, L.-L.; Ma, S.-S.; Li, R.-P.; et al. Engineering 4f-2p-3d orbital hybridization on cerium-doped nickel–molybdenum phosphates for energy-saving hydrogen evolution. *Rare Met.* **2025**, *44*, 1883–1894.
45. Zheng, X.; Li, P.; Dou, S.; et al. Non-carbon-supported single-atom site catalysts for electrocatalysis. *Energy Environ. Sci.* **2021**, *14*, 2809–2858.
46. Chen, F.; Wu, Z.; Gupta, S.; et al. Efficient conversion of low-concentration nitrate sources into ammonia on a Ru-dispersed Cu nanowire electrocatalyst. *Nat. Nanotechnol.* **2022**, *17*, 759–767.
47. Zhou, B.; Yu, L.; Zhang, W.; et al. Cu_1−Fe Dual Sites for Superior Neutral Ammonia Electrosynthesis from Nitrate. *Angew. Chem. Int. Ed.* **2024**, *63*, e202406046.
48. Wang, Q.; Wei, H.; Liu, P.; et al. Recent advances in copper-based catalysts for electrocatalytic CO_2 reduction toward multi-carbon products. *Nano Res. Energy* **2024**, *3*, e9120112.
49. Guo, H.; Guo, Z.; Xue, G.; et al. Entropy-driven stabilization of noble metal single atoms: Advancing ammonia synthesis and energy output in zinc-nitrate batteries. *Adv. Mater.* **2025**, *37*, 2500224.
50. Cai, Y.-M.; Li, Y.-H.; Xiao, Y.; et al. Synergistic rare-earth yttrium single atoms and copper phosphide nanoparticles for high-selectivity ammonia electrosynthesis. *Rare Met.* **2024**, *43*, 5792–5801.
51. Wang, Y.; Hao, F.; Xu, H.; et al. Interfacial water structure modulation on unconventional phase non-precious metal alloy nanostructures for efficient nitrate electroreduction to ammonia in neutral media. *Angew. Chem. Int. Ed.* **2025**, *64*, e202508617.
52. Han, S.; Li, H.; Li, T.; et al. Ultralow overpotential nitrate reduction to ammonia via a three-step relay mechanism. *Nat. Catal.* **2023**, *6*, 402–414.
53. Li, Y.; Zhang, Q.; Dai, H.; et al. Photoelectrochemical nitrate denitrification towards acidic ammonia synthesis on copper-decorated black silicon. *Energy Environ. Sci.* **2024**, *17*, 9233–9243.
54. Zhou, J.; Liu, F.; Xu, Z.; et al. Modulating the nitrate reduction pathway on unconventional phase ultrathin nanoalloys for selective ammonia electrosynthesis. *J. Am. Chem. Soc.* **2025**, *147*, 26, 23226–23238.
55. You, Y.; Chen, H.; Guo, J.; et al. Structure reconstruction driven by oxygen vacancies forming P-$CoMoO_4$/Co $(OH)_2$ heterostructure boosting electrocatalytic nitrate reduction to ammonia. *Appl. Catal. B Environ.* **2025**, *363*, 124837.
56. Wang, H.; Liu, Q.; Chen, K.; et al. Unlocking the coupling potential of built-in electric field and pulsed electroreduction for efficient nitrate to ammonia at low concentrations. *Appl. Catal. B Environ.* **2025**, *374*, 125387.
57. Xu, M.; Dong, S.; Guo, H.; et al. Defective perovskite supported palladium-nickel nanocatalyst for effective electrochemical nitrate reduction. *Appl. Catal. B Environ.* **2025**, *375*, 125433.
58. Wang, R.; Jia, S.; Wu, L.; et al. Tuning the acid hardness nature of Cu catalyst for selective nitrate-to-ammonia electroreduction. *Angew. Chem. Int. Ed.* **2025**, *64*, 15, e202425262.
59. Chao, G.; Zong, W.; Zhu, J.; et al. Selective mass accumulation at the metal–polymer bridging interface for efficient nitrate electroreduction to ammonia and Zn-nitrate batteries. *J. Am. Chem. Soc.* **2025**, *147*, 25, 21432–21442.
60. Li, Z.; Wang, Q.; Zhong, L.; et al. Boosting ammonia electrosynthesis via interfacial tandem nitrate reduction enabled by an amorphous@ crystalline electrocatalyst. *Mater. Today* **2025**, *85*, 49–59.
61. Zhu, G.; Bao, W.; Xie, M.; et al. Accelerating tandem electroreduction of nitrate to ammonia via multi-site synergy in mesoporous carbon-supported high-entropy intermetallics. *Adv. Mater.* **2025**, *37*, 5, 2413560.
62. Wu, T.; Chen, J.; Liu, L.; et al. Three-dimensional Cu_3P/Cu heterostructure as robust tandem electrocatalyst for selective electroreduction of nitrate to ammonia. *Appl. Catal. B Environ.* **2024**, *358*, 124408.
63. Wang, Y.; Xu, A.; Wang, Z.; et al. Enhanced nitrate-to-ammonia activity on copper–nickel alloys via tuning of intermediate adsorption. *J. Am. Chem. Soc.* **2020**, *142*, 12, 5702–5708.
64. Guo, Y.; Zhang, R.; Zhang, S.; et al. Pd doping-weakened intermediate adsorption to promote electrocatalytic nitrate reduction on TiO_2 nanoarrays for ammonia production and energy supply with zinc–nitrate batteries. *Energy Environ. Sci.* **2021**, *14*, 3938–3944.
65. Zhang, H.; Wang, H.; Cao, X.; et al. Unveiling cutting-edge developments in electrocatalytic nitrate-to-ammonia conversion. *Adv. Mater.* **2024**, *36*, 16, 2312746.
66. Cao, Y.; Yuan, S.; Meng, L.; et al. Recent advances in electrocatalytic nitrate reduction to ammonia: Mechanism insight and catalyst design. *ACS Sustain. Chem. Eng.* **2023**, *11*, 21, 7965–7985.
67. Min, B.; Gao, Q.; Yan, Z.; et al. Powering the remediation of the nitrogen cycle: Progress and perspectives of electrochemical nitrate reduction. *Ind. Eng. Chem. Res.* **2021**, *60*, 41, 14635–14650.
68. Vooys, A.; Santen, R.; Veen, J. Electrocatalytic reduction of NO_3^- on palladium/copper electrodes. *J. Mol. Catal. A Chem.* **2000**, *154*, 203–215.

69. Dima, G.; Vooys, A.; Koper, M. Electrocatalytic reduction of nitrate at low concentration on coinage and transition-metal electrodes in acid solutions. *J. Electroanal. Chem.* **2003**, *554*, 15–23.
70. Cheng, Y.; Wang, H.; Song, H.; et al. Design strategies towards transition metal single atom catalysts for the oxygen reduction reaction–A review. *Nano Res. Energy* **2023**, *2*, e9120082.
71. Carvalho, O.; Marks, R.; Nguyen, H.; et al. Role of electronic structure on nitrate reduction to ammonium: A periodic journey. *J. Am. Chem. Soc.* **2022**, *144*, 32, 14809–14818.
72. Guo, H.; Zhang, P.; Huang, S.; et al. Achilles' heel of single atom catalysts towards practical PEMFC application: Degradation mechanisms and regulatory strategies. *Nano Res. Energy* **2025**, *4*, e9120144.
73. Wu, B.; Wang, T.; Liu, B.; et al. Stable solar water splitting with wettable organic-layer-protected silicon photocathodes. *Nat. Commun.* **2022**, *13*, 4460.
74. Jin, W.; Lee, Y.; Shin, C.; et al. Crystalline silicon photocathode with tapered microwire arrays achieving a high current density of 41.7 mA cm^{-2}. *Adv. Mater. Interfaces* **2024**, *11*, 2400178.
75. Tayyebi, A.; Mehrotra, R.; Mubarok, M.A.; et al. Bias-free solar NH_3 production by perovskite-based photocathode coupled to valorization of glycerol. *Nat. Catal.* **2024**, *7*, 510.
76. Chiang, C.-H.; Kao, Y.-T.; Wu, P.-H.; et al. Efficient ammonia photosynthesis from nitrate by graphene/Si Schottky junction integrated with Ni–Fe LDH catalyst. *J. Mater. Chem. A* **2023**, *11*, 11179.
77. Zhou, J.; Wen, M.; Huang, R.; et al. Regulating active hydrogen adsorbed on grain boundary defects of nano-nickel for boosting ammonia electrosynthesis from nitrate. *Energy Environ. Sci.* **2023**, *16*, 2611.
78. Ballif, C.; Haug, F.-J.; Boccard, M.; et al. Status and perspectives of crystalline silicon photovoltaics in research and industry. *Nat. Rev. Mater.* **2022**, *7*, 597.
79. Gao, R.; Zhang, J.; Fan, G.; et al. *In situ* electrochemical reconstruction of cation-vacancy-enriched Ni@Ni_2P particles in hollow N-doped carbon nanofibers for efficient nitrate reduction. *Angew. Chem. Int. Ed.* **2025**, *64*, e202505948.
80. Sui, C.; Jiang, Z.; Higueros, G.; et al. Designing electrodes and electrolytes for batteries by leveraging deep learning. *Nano Res. Energy* **2024**, *3*, e9120102.
81. Wu, Q.; Han, Y.; Wu, L.; et al. Constructing asymmetric Sn-Cu-C interface via defective carbon trapped atomic clusters for efficient neutral nitrate reduction. *Adv. Mater.* **2025**, *37*, 2505743.
82. Yin, H.; He, J.; Xiao, B.; et al. Advances and prospects of g-C_3N_4 in lithium-sulfur batteries. *Nano Res. Energy* **2024**, *3*, e9120138.
83. Jang, D.; Maeng, J.; Kim, J.; et al. Boosting electrocatalytic nitrate reduction reaction for ammonia synthesis by plasma-induced oxygen vacancies over $MnCuO_x$. *Appl. Surf. Sci.* **2023**, *610*, 155521.
84. Messias, I.; Winkler, M.E.G.; Costa, G.F.; et al. Role of structural and compositional changes of Cu_2O nanocubes in nitrate electroreduction to ammonia. *ACS Appl. Energy Mater.* **2024**, *7*, 9034–9044.
85. Liu, D.; Qiao, L.; Peng, S.; et al. Recent advances in electrocatalysts for efficient nitrate reduction to ammonia. *Adv. Funct. Mater.* **2023**, *33*, 2303480.
86. Zhang, B.; Dai, Z.; Chen, Y.; et al. Defect-induced triple synergistic modulation in copper for superior electrochemical ammonia production across broad nitrate concentrations. *Nat. Commun.* **2024**, *15*, 2816.
87. Sun, Y.; Shi, Y.; Gao, Y.; et al. Electroreduction of nitrate into ammonia on Co_3O_4: Mechanistic insights into Co^{2+}-promoted NO_3RR performance. *Chem. Eng. J.* **2025**, *512*, 162506.
88. Maeng, J.; Jang, D.; Ha, J.; et al. Oxygen Vacancy-Controlled CuOx/N, Se Co-Doped Porous Carbon via Plasma-Treatment for Enhanced Electro-Reduction of Nitrate to Green Ammonia. *Small* **2024**, *20*, 2403253.
89. Mei, W.; Chang, C.-W.; Li, Z.; et al. Robust oxygen-vacancy-engineered $Co(OH)_2$/Cu heterostructures boost nitrate electroreduction to ammonia beyond 2 A cm^{-2}. *Adv. Mater.* **2025**, 2507363.
90. Song, M.; Xing, Y.; Li, Y.; et al. Fe and Cu double-doped Co_3O_4 nanorod with abundant oxygen vacancies: A high-rate electrocatalyst for tandem electroreduction of nitrate to ammonia. *Inorg. Chem.* **2023**, *62*, 16641–16651.
91. Bui, T.S.; Lovell, E.C.; Daiyan, R.; et al. Defective metal oxides: Lessons from CO_2RR and applications in NO_xRR. *Adv. Mater.* **2023**, *35*, 2205814.
92. Gu, L.; Cong, Y.; Wu, Z.; et al. Multiscopic microenvironment engineering in nitrate electrocatalytic reduction. *Adv. Funct. Mater.* **2025**, 2500316.
93. Li, H.; Ma, N.; Long, Y.; et al. The electrocatalytic role of oxygen vacancy in nitrate reduction reactions. *ACS Appl. Mater. Interfaces.* **2024**, *16*, 46312–46322.
94. Jeong, Y.J.; Tan, R.; You, T.H.; et al. Boosting nitrate-to-ammonia electrosynthesis via hierarchically branched TiO_2 nanorods. *J. Mater. Chem. A* **2025**, *13*, 28295–28304.
95. Lv, Y.; Ren, J.; Jiang, M.; et al. A-site deficiency-mediated creation of oxygen vacancies in $LaMnO_{3-\delta}$ nanofibers for efficient nitrate reduction. *ACS Catal.* **2025**, *15*, 8094–8102.
96. Deng, Z.-W.; Liu, Y.; Lin, J.; et al. Rational design and energy catalytic application of high-loading single-atom catalysts. *Rare Met.* **2024**, *43*, 4844–4866.

97. Yang, L.-H.; Lin, Z.-Q.; Yu, C.-H.; et al. Polarity-inverted perovskite $LaFeO_3$ promotes nitrate electroreduction by intensifying the adsorption effect. *J. Mater. Sci. Technol.* **2026**, *245*, 164–174.
98. Wu, Q.; Fan, X.; Shan, B.; et al. Insights into lattice oxygen and strains of oxide-derived copper for ammonia electrosynthesis from nitrate. *Nat. Commun.* **2025**, *16*, 3479.
99. Yoon, A.; Bai, L.; Yang, F.; et al. Revealing catalyst restructuring and composition during nitrate electroreduction through correlated *operando* microscopy and spectroscopy. *Nat. Mater.* **2025**, *24*, 762–769.
100. Fu, W.; Yin, Y.; He, S.; et al. Electrocatalytic conversion of nitrate to ammonia on the oxygen vacancy engineering of zinc oxide for nitrogen recovery from nitrate-polluted surface water. *Environ. Res.* **2025**, *264*, 120279.
101. Li, P.; Li, R.; Liu, Y.; et al. Pulsed nitrate-to-ammonia electroreduction facilitated by tandem catalysis of nitrite intermediates. *J. Am. Chem. Soc.* **2023**, *145*, 6471.
102. Zhang, S.; Li, M.; Li, J.; et al. High-ammonia selective metal–organic framework–derived Co-doped Fe/Fe_2O_3 catalysts for electrochemical nitrate reduction. *Proc. Natl. Acad. Sci. USA* **2022**, *119*, 2115504119.
103. Li, J.; Chen, R.; Wang, J.; et al. Subnanometric alkaline-earth oxide clusters for sustainable nitrate to ammonia photosynthesis. *Nat. Commun.* **2022**, *13*, 1098.
104. Wei, Q.; He, Y.; Ding, G.; et al. Pd orbital hybridization and lattice strain induced by B, Co-co-doped Cu promote the electrocatalytic nitrate reduction to ammonia. *Chem. Eng. J.* **2025**, *508*, 161014.
105. Xu, Y.; Sheng, Y.; Wang, M.; et al. Lattice-strain and Lewis acid sites synergistically promoted nitrate electroreduction to ammonia over PdBP nanothorn arrays. *J. Mater. Chem. A* **2022**, *10*, 16290–16296.
106. Gao, Q.; Yao, B.; Liu, Y.; et al. Strain relaxation enhances ammonia electrosynthesis from nitrate on Cu/CuAu core/shell nanocrystals with ordered intermetallic layers. *Chem. Catal.* **2025**, *5*, 101328.
107. Wang, Y.; Hao, F.; Sun, M.; et al. Crystal phase engineering of ultrathin alloy nanostructures for highly efficient electroreduction of nitrate to ammonia. *Adv. Mater.* **2024**, *36*, 2313548.
108. Liu, S.; Miao, W.; Ma, K.; et al. Defect-rich AuCu@Ag nanowires with exclusive strain effect accelerate nitrate reduction to ammonia. *Appl. Catal. B Environ. Energy* **2024**, *350*, 123919.
109. Fu, Y.; Wang, S.; Wang, Y.; et al. Enhancing electrochemical nitrate reduction to ammonia over Cu nanosheets via facet tandem catalysis. *Angew. Chem. Int. Ed.* **2023**, *62*, e202303327.
110. Liu, H.; Jia, S.; Wu, L.; et al. Circumventing scaling relations via gradient orbital coupling promotes ammonia electrosynthesis on Cobalt catalyst. *Angew. Chem. Int. Ed.* **2025**, *64*, e202510478.
111. Liu, J.; Xu, Y.; Duan, R.; et al. Reaction-driven formation of anisotropic strains in FeTeSe nanosheets boosts low-concentration nitrate reduction to ammonia. *Nat. Commun.* **2025**, *16*, 3595.
112. Liu, Z.; Li, Y.-Q.; Tan, Y.-F.; et al. Sulfur-modulated charge-asymmetry Cu–Zn bimetallic nanoclusters for efficient CO_2 electroreduction. *Rare Met.* **2025**, *44*, 6211–6222.
113. Yang, Y.; Zhang, W.; Wu, G.; et al. Electronic structure tuning in Cu–Co dual single atom catalysts for enhanced COOH* spillover and electrocalytic CO_2 reduction activity. *Angew. Chem. Int. Ed.* **2025**, *64*, 23, e202504423.
114. Gao, Q.; Pillai, H.S.; Huang, Y.; et al. Breaking adsorption-energy scaling limitations of electrocatalytic nitrate reduction on intermetallic CuPd nanocubes by machine-learned insights. *Nat. Commun.* **2022**, *13*, 2338.
115. Lu, Y.; Yue, F.; Liu, T.; et al. Size-effect induced controllable Cu^0-Cu^+ sites for ampere-level nitrate electroreduction coupled with biomass upgrading. *Nat. Commun.* **2025**, *16*, 2392.
116. Liu, X.; Wang, Y.; Hu, Z.; et al. Self-reducing Cu_2O/Cu nanosheet interface for efficient electrocatalytic production of ammonium from nitrate. *Appl. Catal. B Environ. Energy* **2025**, *371*, 125254.
117. Li, J.; Liu, L.; Huang, S.; et al. Nanoflower-Like CuPd/CuO heterostructure for an energy-output electrocatalytic system coupling ammonia electrosynthesis and zinc-nitrate battery. *Adv. Funct. Mater.* **2025**, *35*, 2501527.
118. Zheng, S.; Yang, X.; Shi, Z.-Z.; et al. The loss of interfacial water-adsorbate hydrogen bond connectivity position surface-active hydrogen as a crucial intermediate to enhance nitrate reduction reaction. *J. Am. Chem. Soc.* **2024**, *146*, 26965–26974.
119. Li, X.; Rong, H.; Zhang, J.; et al. Modulating the local coordination environment of single-atom catalysts for enhanced catalytic performance. *Nano Res.* **2020**, *13*, 7, 1842–1855.
120. Fei, H.; Dong, J.; Chen, D.; et al. Single atom electrocatalysts supported on graphene or graphene-like carbons. *Chem. Soc. Rev.* **2019**, *48*, 20, 5207–5241.
121. Gong, Y.; Jiao, L.; Qian, Y.; et al. Regulating the coordination environment of MOF-templated single-atom nickel electrocatalysts for boosting CO_2 reduction. *Angew. Chem. Int. Ed.* **2020**, *59*, 7, 2705–2709.
122. Liang, J.; Yu, Q.; Yang, X.; et al. A systematic theoretical study on FeO_x-supported single-atom catalysts: M_1/FeO_x for CO oxidation. *Nano Res.* **2018**, *11*, 3, 1599–1611.
123. Zhang, W.; Zhao, Y.; Huang, W.; et al. Coordination environment manipulation of single atom catalysts: Regulation strategies, characterization techniques and applications. *Coordin. Chem. Rev.* **2024**, *515*, 215952.

124. Zhu, Y.; Sokolowski, J.; Song, X.; et al. Engineering local coordination environments of atomically dispersed and heteroatom-coordinated single metal site electrocatalysts for clean energy-conversion. *Adv. Energy Mater.* **2020**, *10*, 11, 1902844.
125. Gao, Y.; Liu, B.; Wang, D. Microenvironment engineering of single/dual-atom catalysts for electrocatalytic application. *Adv. Mater.* **2023**, *35*, 31, 2209654.
126. Wu, X.; Zhang, H.; Zuo, S.; et al. Engineering the coordination sphere of isolated active sites to explore the intrinsic activity in single-atom catalysts. *Nano-Micro Lett.* **2021**, *13*, 136.
127. Liu, W.; Zhang, L.; Liu, X.; et al. Discriminating catalytically active FeN_x species of atomically dispersed Fe–N–C catalyst for selective oxidation of the C–H bond. *J. Am. Chem. Soc.* **2017**, *139*, 31, 10790–10798.
128. Du, J., Lin, Q.Y., Zhang, J.Q.; et al. N-doped core–shell mesoporous carbon spheres embedded by Ni nanoparticles for CO_2 electroreduction. *Rare Met.* **2023**, *42*, 2284–2293.
129. Jakub, Z.; Hulva, J.; Meier, M.; et al. Local structure and coordination define adsorption in a model Ir_1/Fe_3O_4 single-atom catalyst. *Angew. Chem. Int. Ed.* **2019**, *58*, 39, 13961–13968.
130. Chen, J.; Xiao, Y.; Da, Y.; et al. Mechanistic insights and advances in electrode/electrolyte interfaces for efficient electrocatalytic CO_2 reduction to C_2 products. *SmartMat* **2025**, *6*, e1324.
131. Wang, Z.; Hao, X.; Jiang, Z.; et al. C and N hybrid coordination derived Co–C–N complex as a highly efficient electrocatalyst for hydrogen evolution reaction. *J. Am. Chem. Soc.* **2015**, *137*, 48, 15070–15073.
132. Yang, Q.; Jia, Y.; Wei, F.; et al. Understanding the activity of Co-$N_{4-x}C_x$ in atomic metal catalysts for oxygen reduction catalysis. *Angew. Chem. Int. Ed.* **2020**, *59*, 15, 6122–6127.
133. Chen, W.; Pei, J.; He, C.; et al. Single tungsten atoms supported on MOF-derived N-doped carbon for robust electrochemical hydrogen evolution. *Adv. Mater.* **2018**, *30*, 30, 1800396.
134. Wang, Y.; Zhang, W.; Wen, W.; et al. Atomically dispersed unsaturated Cu-N_3 sites on high-curvature hierarchically porous carbon nanotube for synergetic enhanced nitrate electroreduction to ammonia. *Adv. Funct. Mater.* **2023**, *33*, 2302651.
135. Liu, K.; Sun, Z.; Peng, X.; et al. Tailoring asymmetric RuCu dual-atom electrocatalyst toward ammonia synthesis from nitrate. *Nat. Commun.* **2025**, *16*, 2167.
136. Talib, S.H.; Jiang, X.; Feng, S.; et al. Theoretical catalytic performance of single-atom catalysts $M_1/PW_{12}O_{40}$ for alkyne hydrogenation materials. *Nano Res. Energy* **2024**, *3*, e9120128.
137. Yin, L.; Zhang, S.; Sun, M.; et al. Heteroatom-driven coordination fields altering single cerium atom sites for efficient oxygen reduction reaction. *Adv. Mater.* **2023**, *35*, 28, 2302485.
138. Yang, J.; Wang, M.; Gao, S.; et al. Proton driving mechanism revealed in sulfur-doped single-atom FeN_2O_2 carbon dots for superior peroxidase activity. *Angew. Chem. Int. Ed.* **2025**, *64*, 30, e202504575.
139. Ci, H.; Shi, Z.; Wang, M.; et al. A review in rational design of graphene toward advanced Li–S batteries. *Nano Res. Energy* **2023**, *2*, e9120054.
140. Xu, J.; Zhang, S.; Liu, H.; et al. Breaking local charge symmetry of iron single atoms for efficient electrocatalytic nitrate reduction to ammonia. *Angew. Chem. Int. Ed.* **2023**, *62*, 39, e202308044.
141. Ajmal, S.; Kumar, A.; Mushtaq, M.; et al. Uniting synergistic effect of single-Ni site and electric field of B-Bridged-N for boosted electrocatalytic nitrate reduction to ammonia. *Small* **2024**, *20*, 32, 2310082.
142. Jin, H.-L.; Li, Q.-N.; Tian, Y.-Y.; et al. Machine-learning-aided Au-based single-atom alloy catalysts discovery for electrochemical NO reduction reaction to NH_3. *Rare Met.* **2024**, *43*, 5813–5822.
143. Wu, Q.; Fan, X.; Liu, K.; et al. Efficient and selective electroreduction of nitrate to ammonia via interfacial engineering of B-doped Cu nanoneedles. *Appl. Catal. B Environ.* **2025**, *361*, 124597.
144. Wang, Z.; Lian, X.; Yang, R.; et al. Planar chlorination engineering enhances the polarity of the Fe–N_4 site for boosting nitrate electroreduction. *ACS Catal.* **2025**, *15*, 8230–8238.
145. Xiang, J.; Wang, P.; Li, P.; et al. Inter-site distance effect in electrocatalysis. *Angew. Chem. Int. Ed.* **2025**, *64*, e202500644.
146. Hu, C.; Zhang, Y.; Hu, A.; et al. Near-and long-range electronic modulation of single metal sites to boost CO_2 electrocatalytic reduction. *Adv. Mater.* **2023**, *35*, 2209298.
147. Zhang, S.; Wu, J.; Zheng, M.; et al. Fe/Cu diatomic catalysts for electrochemical nitrate reduction to ammonia. *Nat. Commun.* **2023**, *14*, 3634.
148. Chen, Z.; Sang, K.; Ye, L.; et al. Tandem switch-triggered on-demand synthesis of aromatic amines in high yields. *Angew. Chem. Int. Ed.* **2025**, *64*, 18, e202424847.
149. Luo, W.; Liu, K.; Luo, T.; et al. Promoting C–F bond activation for perfluorinated compounds decomposition via atomically synergistic Lewis and Brønsted acid sites. *J. Am. Chem. Soc.* **2025**, *147*, 9, 7391–7399.
150. Wang, Y.; Wang, C.; Li, M.; et al. Nitrate electroreduction: Mechanism insight, *in situ* characterization, performance evaluation, and challenges. *Chem. Soc. Rev.* **2021**, *50*, 6720–6733.

151. Jia, R.; Wang, Y.; Wang, C.; et al. Boosting selective nitrate electroreduction to ammonium by constructing oxygen vacancies in TiO_2. *ACS Catal.* **2020**, *10*, 3533–3540.
152. Yan, K.; Ge, X.; Cao, Y.; et al. Pd ensemble sites tuned local environment of Cu catalysts for matching propyne semi-hydrogenation. *Angew. Chem. Int. Ed.* **2025**, *64*, 19, e202503263.
153. Wang, L.; Gui, W.-K.; Jiang, S.; et al. Bi_2S_3 nanofiber bunch for highly efficient CO_2 electroreduction to formate at low overpotential. *Rare Met.* **2024**, *43*, 3391–3399.
154. Morales, C.; Cave, E.; Nitopi, S.; et al. Improved CO_2 reduction activity towards C_{2+} alcohols on a tandem gold on copper electrocatalyst. *Nat. Catal.* **2018**, *1*, 764–771.
155. Lou, Y.; Zheng, Q.; Zhou, S.; et al. Phase-dependent electrocatalytic nitrate reduction to ammonia on Janus Cu@ Ni tandem catalyst. *ACS Catal.* **2024**, *14*, 7, 5098–5108.
156. Li, X.; Shen, P.; Li, X.; et al. Sub-nm RuO_x clusters on Pd metallene for synergistically enhanced nitrate electroreduction to ammonia. *ACS Nano* **2023**, *17*, 2, 1081–1090.
157. Li, J.; Hu, J.; Zhang, M.; et al. A fundamental viewpoint on the hydrogen spillover phenomenon of electrocatalytic hydrogen evolution. *Nat. Commun.* **2021**, *12*, 3502.
158. Feng, J.; Hu, Q.; Yue, X.; et al. Bimetallic phthalocyanine catalyst for ammonia electrosynthesis from nitrate reduction across all pH ranges. *Appl. Catal. B Environ. Energy* **2025**, *366*, 125027.
159. Zhu, J.; Hu, L.; Zhao, P.; et al. Recent advances in electrocatalytic hydrogen evolution using nanoparticles. *Chem. Rev.* **2020**, *120*, 2, 851–918.
160. Xiao, H.; Lv, Y.; Hua, W.; et al. Atomically dispersed dual frustrated Lewis pairs for efficient relay conversion of nitrate into ammonia. *Appl. Catal. B Environ.* **2025**, *377*, 125501.
161. Wan, J.; Zhang, H.; Yang, J.; et al. Synergy between Fe and Mo single atom catalysts for ammonia electrosynthesis. *Appl. Catal. B Environ.* **2024**, *347*, 123816.
162. Shen, F.; He, S.; Tang, X.; et al. Breaking linear scaling relation limitations on a dual-driven single-atom copper-tungsten oxide catalyst for ammonia synthesis. *Angew. Chem. Int. Ed.* **2025**, *64*, 21, e202423154.
163. Chen, H.; Qi, K.; Dong, X.; et al. Ligand-mediated activity of Cu_4 clusters boosts electrocatalytic nitrate reduction. *Angew. Chem. Int. Ed.* **2025**, *64*, e202510429. https://doi.org/10.1002/anie.202510429.
164. Zhang, L.; Cai, Y.; Li, Y.; et al. Unlocking high-current-density nitrate reduction and formaldehyde oxidation synergy for scalable ammonia production and fixation. *Energy Environ. Sci.* **2025**, *18*, 6, 2804–2816.
165. Wan, J.; Yang, J.; Yang, N.; et al. Axial chlorine-induced symmetry-breaking iron single-atom catalyst for electrochemical ammonia synthesis. *ACS Catal.* **2025**, *15*, 6, 4507–4518.
166. Guan, J.; Cai, L.; Li, W.; et al. Boosting nitrate electroreduction to ammonia on atomic Ru-Co pair sites in hollow spinels. *Appl. Catal. B Environ.* **2024**, *358*, 124387.
167. Xia, J.; Xu, J.; Yu, B.; et al. A metal–sulfur–carbon catalyst mimicking the two-component architecture of nitrogenase. *Angew. Chem. Int. Ed.* **2024**, *63*, 45, e202412740.
168. Wang, B.; Ma, J.; Yang, R.; et al. Bridging nickel-MOF and copper single atoms/clusters with H-substituted graphdiyne for the tandem catalysis of nitrate to ammonia. *Angew. Chem. Int. Ed.* **2024**, *63*, 30, e202404819.
169. Liu, Y.; Zhuang, Z.; Liu, Y.; et al. Shear-strained Pd single-atom electrocatalysts for nitrate reduction to ammonia. *Angew. Chem. Int. Ed.* **2024**, *63*, 43, e202411396.
170. Zhao, Z.; Yang, S.; Wang, S.; et al. Isolated rhodium atoms activate porous TiO_2 for enhanced electrocatalytic conversion of nitrate to ammonia. *Adv. Sci.* **2025**, *12*, 2, 2411705.
171. Park, J.; Theerthagiri, J.; Yodsin, N.; et al. CO_2 laser-stabilized Ni-Co dual single-atomic sites for energy generation and ammonia harvesting. *Adv. Mater.* **2025**, *37*, 30, 2506137.
172. Zhong, W.; Hong, Q.; Ai, X.; et al. RhNi bimetallenes with lattice-compressed Rh skin towards ultrastable acidic nitrate electroreduction. *Adv. Mater.* **2024**, *36*, 23, 2314351.
173. Messe, A.; Napier, C.; Kim, D.; et al. Underpotential deposition of 3D transition metals: Versatile electrosynthesis of single-atom catalysts on oxidized carbon supports. *Adv. Mater.* **2024**, *36*, 19, 2311341.
174. Zhang, Y.; Zheng, H.; Zhou, K.; et al. Conjugated coordination polymer as a new platform for efficient and selective electroreduction of nitrate into ammonia. *Adv. Mater.* **2023**, *35*, 10, 2209855.
175. Ni, J.; Yan, J.; Li, F.; et al. Atomic Co-P catalytic pair drives efficient electrochemical nitrate reduction to ammonia. *Adv. Energy Mater.* **2024**, *14*, 28, 2400065.
176. Zhang, S.; Li, K.; Zhang, X.; et al. Concurrently selective electrosynthesis of ammonia and glycolic acid over cathodic single-atom cobalt and anodic PdNi alloying catalysts. *Adv. Funct. Mater.* **2025**, *35*, 6, 2415046.
177. Song, J.; Qian, S.; Yang, W.; et al. Nano-single-atom heterointerface engineering for pH-universal electrochemical nitrate reduction to ammonia. *Adv. Funct. Mater.* **2024**, *34*, 49, 2409089.
178. Lin, H.; Wei, J.; Guo, Y.; et al. Bi_1-$CuCo_2O_4$ hollow carbon nanofibers boosts NH_3 production from electrocatalytic nitrate reduction. *Adv. Funct. Mater.* **2024**, *34*, 51, 2409696.

179. Zhang, N.; Zhang, G.; Shen, P.; et al. Lewis acid Fe-V pairs promote nitrate electroreduction to ammonia. *Adv. Funct. Mater.* **2023**, *33*, 13, 2211537.
180. Zhang, G.; Wang, F.; Chen, K.; et al. Atomically dispersed Sn confined in FeS_2 for nitrate-to-ammonia electroreduction. *Adv. Funct. Mater.* **2024**, *34*, 1, 2305372.
181. Liu, L.; Xiao, T.; Fu, H.; et al. Construction and identification of highly active single-atom Fe_1-NC catalytic site for electrocatalytic nitrate reduction. *Appl. Catal. B Environ. Energy* **2023**, *323*, 122181.
182. Yu, J.; Gao, R.; Guo, X.; et al. Electrochemical nitrate reduction to ammonia on AuCu single-atom alloy aerogels under wide potential window. *Angew. Chem. Int. Ed.* **2025**, *64*, 4, e202415975.
183. Xie, M.; Tang, S.; Li, Z.; et al. Intermetallic single-atom alloy In–Pd bimetallene for neutral electrosynthesis of ammonia from nitrate. *J. Am. Chem. Soc.* **2023**, *145*, 25, 13957–13967.
184. Ji, X.; Sun, K.; Liu, Z.; et al. Identification of dynamic active sites among Cu species derived from MOFs@ CuPc for electrocatalytic nitrate reduction reaction to ammonia. *Nano-Micro Lett.* **2023**, *15*, 1, 110.
185. Xiang, T.; Liu, X.; Wang, Z.; et al. Boosting active hydrogen generation via ruthenium single atoms for efficient electrocatalytic nitrate reduction to ammonia. *Appl. Catal. B Environ.* **2025**, *365*, 124943.
186. Li, Q.; Ma, Y.; Zeng, Q.; et al. Coupling ZnN_4 atomic sites with graphitic nitrogen for enhanced ammonium production via electrocatalytic nitrate reduction. *Small* **2025**, *21*, 6, 2409925.
187. Wei, J.; Lin, H.; Li, Y.; et al. Cobalt-copper dual-atom catalyst boosts electrocatalytic nitrate reduction from water. *J. Hazard. Mater.* **2025**, *493*, 138264.
188. Liu, Y.; Qiu, W.; Wang, P.; et al. Pyridine-N-rich Cu single-atom catalyst boosts nitrate electroreduction to ammonia. *App. Catal. B Environ.* **2024**, *340*, 123228.
189. Weng, Z.; Wu, Y.; Wang, M.; et al. Active sites of copper-complex catalytic materials for electrochemical carbon dioxide reduction. *Nat. Commun.* **2018**, *9*, 415.
190. Ren, Y.; Tian, F.; Jin, L.; et al. Fluidic MXene electrode functionalized with iron single atoms for selective electrocatalytic nitrate transformation to ammonia. *Environ. Sci. Technol.* **2023**, *57*, 28, 10458–10466.
191. Ren, Y.; Wang, J.; Yang, L.; et al. Single-atom Cu and Zn vacancy synergy in NiFe-LDH boosts metal–support interaction for high-efficiency nitrate-to-ammonia electroreduction. *Environ. Sci. Technol.* **2025**, *59*, 22, 11414–11425.
192. Zhang, H.; Liu, Y.; Gao, S.; et al. Atomically dispersed iron & iron clusters synergistically accelerate electrocatalytic ammonia synthesis. *Chem. Eng. J.* **2025**, *504*, 158785.
193. Hao, J.; Wang, T.; Yu, R.; et al. Integrating few-atom layer metal on high-entropy alloys to catalyze nitrate reduction in tandem. *Nat. Commun.* **2024**, *15*, 9020.
194. Yan, Z.; Gao, W.; Zhong, C.; et al. Regulating spin state of Fe (III) by the Mo single atom anchored in the (001) crystal face of α-Fe_2O_3 to achieve efficient electrocatalytic nitrate to synthesize ammonia. *Appl. Catal. B Environ.* **2025**, *366*, 125008.
195. Chen, K.; Ma, Z.; Li, X.; et al. Single-atom Bi alloyed Pd metallene for nitrate electroreduction to ammonia. *Adv. Funct. Mater.* **2023**, *33*, 12, 2209890.
196. Wang, Y.; Yin, H.; Dong, F.; et al. N-coordinated Cu–Ni dual-single-atom catalyst for highly selective electrocatalytic reduction of nitrate to ammonia. *Small* **2023**, *19*, 20, 2207695.
197. Li, Q.; Li, Y.; Xu, B.; et al. Gram-scale ammonia synthesis via electrochemical nitrate reduction using enzyme-inspired dual-atomic Cu catalyst. *Angew. Chem. Int. Ed.* **2025**, *64*, e202510139.
198. Zhao, X.; Geng, Q.; Dong, F.; et al. Boosting the selectivity and efficiency of nitrate reduction to ammonia with a single-atom Cu electrocatalyst. *Chem. Eng. J.* **2023**, *466*, 143314.
199. Duan, W.; Chen; Zhu, Y.; et al. Synergistic effects of Co single atoms and Co nanoparticles for electrocatalytic nitrate-to-ammonium conversion in strongly acidic wastewater. *Appl. Catal. B Environ.* **2025**, *363*, 124812.
200. Du, C.; Lu, S.; Wang, J.; et al. Selectively reducing nitrate into NH_3 in neutral media by PdCu single-atom alloy electrocatalysis. *ACS Catal.* **2023**, *13*, 16, 10560–10569.
201. Gu, Z.; Zhang, Y.; Fu, Y.; et al. Coordination desymmetrization of copper single-atom catalyst for efficient nitrate reduction. *Angew. Chem. Int. Ed.* **2024**, *63*, 38, e202409125.
202. Zhang, S.; Liu, Y.; Ding, Y.; et al. Rational ligand design of conjugated coordination polymers for efficient and selective nitrate electroreduction to ammonia. *Adv. Mater.* **2025**, *37*, 27, 2418681.
203. Wang, Z.; Yi, Z.; Wong, L.; et al. Oxygen doping cooperated with Co-N-Fe dual-catalytic sites: Synergistic mechanism for catalytic water purification within nanoconfined membrane. *Adv. Mater.* **2024**, *36*, 30, 2404278.
204. Yang, L.; Wang, C.; Li, Y.; et al. Frustrated Lewis pairs on Zr single atoms supported N-doped TiO_{2-x} catalysts for electrochemical nitrate reduction to ammonia. *Adv. Funct. Mater.* **2024**, *34*, 36, 2401094.
205. Zhao, T.; Chen, K.; Xu, X.; et al. Homonuclear dual-atom catalysts embedded on N-doped graphene for highly efficient nitrate reduction to ammonia: From theoretical prediction to experimental validation. *Appl. Catal. B Environ. Energy* **2023**, *339*, 123156.

206. Shen, Z.; Yu, Y.; Zhao, Z.; et al. N, O trans-coordinating silver single-atom catalyst for robust and efficient ammonia electrosynthesis from nitrate. *Appl. Catal. B Environ.* **2023**, *331*, 122687.
207. Zhang, A.; Liang, Y.; Zhang, H.; et al. Doping regulation in transition metal compounds for electrocatalysis. *Chem. Soc. Rev.* **2021**, *50*, 17, 9817–9844.
208. Wang, K.; Mao, R.; Liu, R.; et al. Intentional corrosion-induced reconstruction of defective NiFe layered double hydroxide boosts electrocatalytic nitrate reduction to ammonia. *Nat. Water.* **2023**, *1*, 1068–1078.
209. Wang, T.; Tao, L.; Zhu, X.; et al. Combined anodic and cathodic hydrogen production from aldehyde oxidation and hydrogen evolution reaction. *Nat. Catal.* **2022**, *5*, 66–73.
210. Zhong, D.; Gong, Y.; Zhang, C.; et al. Dinuclear metal synergistic catalysis for energy conversion. *Chem. Soc. Rev.* **2023**, *52*, 9, 3170–3214.
211. Cai, Z.; Zhou, D.; Wang, M.; et al. Introducing Fe^{2+} into nickel–iron layered double hydroxide: Local structure modulated water oxidation activity. *Angew. Chem. Int. Ed.* **2018**, *57*, 30, 9392–9396.
212. Wei, C.; Feng, Z.; Baisariyev, M.; et al. Valence change ability and geometrical occupation of substitution cations determine the pseudocapacitance of spinel ferrite XFe_2O_4 (X = Mn, Co, Ni, Fe). *Chem. Mater.* **2016**, *28*, 12, 4129–4133.
213. Wang, D.; Zhou, J.; Hu, Y.; et al. *In Situ* X-ray absorption near-edge structure study of advanced $NiFe(OH)_x$ electrocatalyst on carbon paper for water oxidation. *J. Phys. Chem. C* **2015**, *119*, 34, 19573–19583.
214. Tylus, U.; Jia, Q.; Strickland, K.; et al. Elucidating oxygen reduction active sites in pyrolyzed metal–nitrogen coordinated non-precious-metal electrocatalyst systems. *J. Phys. Chem. C* **2014**, *118*, 17, 8999–9008.
215. Wang, X.; Cullen, D.; Pan, Y.; et al. Nitrogen-coordinated single cobalt atom catalysts for oxygen reduction in proton exchange membrane fuel cells. *Adv. Mater.* **2018**, *30*, 11, 1706758.
216. Wan, Y.; Tang, Y.; Zuo, Y.; et al. Interfacial hydrogen-bond modulation of dynamic catalysts for nitrate electroreduction to ammonia. *Energy Environ. Sci.* **2025**, *18*, 7460–7469.
217. Zhong, J.; Duan, H.; Cai, M.; et al. Cascade electrocatalytic reduction of nitrate to ammonia using bimetallic covalent organic frameworks with tandem active sites. *Angew. Chem. Int. Ed.* **2025**, *137*, e202507956.
218. Li, X.; Xia, S.; Yang, S.; et al. Asymmetric manganese sites in covalent organic frameworks for efficient nitrate-to-ammonia electrocatalysis. *Angew. Chem. Int. Ed.* **2025**, *64*, 29, e202507479.
219. Pan, F.; Fang, L.; Li, B.; et al. N and OH-immobilized Cu_3 clusters *in situ* reconstructed from single-metal sites for efficient CO_2 electromethanation in bicontinuous mesochannels. *J. Am. Chem. Soc.* **2024**, *146*, 2, 1423–1434.
220. Ding, Z.; Pang, Y.; Ma, A.; et al. Single-atom catalysts based on two-dimensional metalloporphyrin monolayers for electrochemical nitrate reduction to ammonia by first-principles calculations and interpretable machine learning. *Int. J. Hydrogen Energy* **2024**, *80*, 586–598.
221. Lv, L.; Shen, Y.; Zhou, M.; et al. High-throughput screening for efficient dual-atom catalysts in electrocatalytic nitrate reduction to ammonia via dissociation–association mechanism. *J. Mater. Chem. A* **2024**, *12*, 6733–6746.